



Flow above the free end of a surface-mounted finite-height circular cylinder: A review



D. Sumner*

Department of Mechanical Engineering, University of Saskatchewan, 57 Campus Drive, Saskatoon, Saskatchewan, Canada S7N 5A9

ARTICLE INFO

Article history:

Received 19 March 2013

Accepted 11 August 2013

Available online 26 September 2013

Keywords:

Bluff body

Finite circular cylinder

Free end

Separated flow

Recirculation zone

Vortex structures

Reattachment

ABSTRACT

The wake of a surface-mounted finite-height circular cylinder and the associated vortex patterns are strongly dependent on the cylinder aspect ratio and the thickness of the boundary layer on the ground plane relative to the dimensions of the cylinder. Above a critical aspect ratio, the mean wake is characterized by streamwise tip vortex structures and Kármán vortex shedding from the sides of the cylinder. Below a critical aspect ratio, a unique mean wake structure is observed. Recent experimental studies in the literature that used phase-averaged techniques, as well as recent numerical simulations, have led to an improved physical understanding of the near-wake vortex flow patterns. However, the flow above the free end of the finite circular cylinder, and its relationship to the near wake, has not been systematically studied. The effects of aspect ratio and boundary layer thickness on the free-end flow field are also not completely understood, nor has the influence of Reynolds number on the free-end flow field been fully explored. Common features associated with the free end include separation from the leading edge, a mean recirculation zone containing a prominent cross-stream arch (or mushroom) vortex, and reattachment onto the free-surface. Other flow features that remain to be clarified include a separation bubble near the leading edge, one or two cross-stream vortices within this separation bubble, the origins of the streamwise tip or trailing vortices, and various critical points in the near-surface flow topology. This paper reviews the current understanding of the flow above the free end of a surface-mounted finite-height circular cylinder, with a focus on models of the flow field, surface oil flow visualization studies, pressure and heat flux distributions on the free-end surface, measurements of the local velocity field, and numerical simulations, found in the literature.

© 2013 Elsevier Ltd. All rights reserved.

1. Introduction

The flow around a surface-mounted finite-height circular cylinder is encountered in many engineering applications, such as antennas, simplified buildings, cooling towers, fuel and gas storage tanks, and chimney stacks. A schematic of the flow around a surface-mounted finite-height circular cylinder is shown in Fig. 1, for a cylinder of diameter D and height H , where x is the streamwise coordinate, y is the cross-stream coordinate, z is the vertical coordinate. Here, the cylinder is mounted normal to a ground plane and is partially immersed in a flat-plate boundary layer, where $\bar{U}(z)$ is the incoming mean flow velocity profile, U_∞ is the freestream velocity outside the boundary layer on the ground plane, and δ is the thickness of the boundary layer.

* Tel.: +1 306 966 5537.

E-mail address: david.sumner@usask.ca

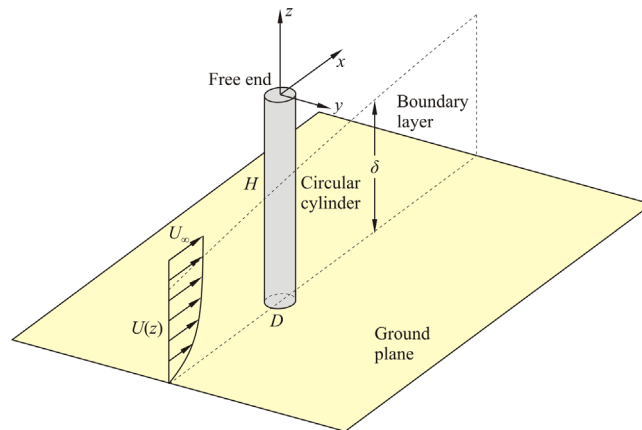


Fig. 1. Schematic of the flow around a surface-mounted finite-height circular cylinder partially immersed in the flat-plate boundary layer on the ground plane. Note the origin of the coordinate system at the center of the free end.

Flow over the circular cylinder's free end and flow around the cylinder-wall junction cause the local flow field and the cylinder's wake to become strongly three-dimensional. In addition to the familiar Kármán vortex shedding from the sides of the cylinder, the flow field is also characterized by the horseshoe (or necklace) vortex forming upstream at the cylinder-wall junction, and two sets of time-averaged streamwise counter-rotating vortex pairs within the wake, one near the free end (the tip or trailing vortices) associated with a downwash flow on the wake centerline (e.g., Kawamura et al., 1984a; Johnston and Wilson, 1996; Adaramola et al., 2006) and the other near the ground plane (the junction or base vortices) (e.g., Tanaka and Murata, 1999; Sumner et al., 2004). Other mean vortex structures may also be found in the recirculation zone in the cylinder's near wake, including a stationary cross-stream mean vortex immediately downstream and below the free end and a second mean cross-stream vortex near the ground plane immediately behind the cylinder-wall junction (e.g., Krajnović, 2011; Rostamy et al., 2012).

Apart from the Reynolds number, $Re = U_\infty D / \nu$ (where ν is the kinematic viscosity), the wake of the finite circular cylinder is strongly influenced by several other parameters, including the cylinder aspect ratio (or slenderness ratio) $AR = H/D$, the approach velocity profile on the ground plane, $\bar{U}(z)/U_\infty$, and the relative thickness of the boundary layer on the ground plane, i.e., the ratios δ/D or δ/H . Many studies in the literature (e.g., Okamoto and Yagita, 1973; Sakamoto and Arie, 1983; Lee, 1997; Sumner et al., 2004; Adaramola et al., 2006) have shown the existence of a critical aspect ratio below which the cylinder has a distinct wake structure; this distinct flow behavior has often been referred to as symmetric “arch vortex shedding” (e.g., Taniguchi et al., 1981; Okamoto and Sunabashiri, 1992; Lee, 1997), which is distinct from the more familiar antisymmetric Kármán vortex shedding. From the various studies in the literature, the value of the critical aspect ratio appears to be sensitive to experimental conditions (values from $AR = 1$ – 7 are quoted in the literature, depending on the study, which is a very wide range), in particular the relative thickness of the boundary layer on the ground plane (Sumner et al., 2004). However, the critical aspect ratio is only loosely defined based on which wake flow pattern is being observed; there have been very few systematic studies of AR effects using small incremental changes in AR to see what happens at the critical value.

Recently, several studies have advanced the physical understanding of the complex vortex patterns in the wake of surface-mounted bluff bodies, moving beyond time-averaged representations of the wake to consider phase-averaged and instantaneous representations of the flow, with emphasis mostly on surface-mounted finite-height square prisms (as opposed to circular cylinders). Taken together, the studies of Wang et al. (2006), Wang and Zhou (2009), Bourgeois et al. (2011), Krajnović (2011), Chen et al. (2012), Sattari et al. (2012), and Wang et al. (2012) offer new physical explanations for the behavior of the streamwise tip and base vortex structures, the Kármán vortices, and the influences of aspect ratio, boundary layer thickness, and the type of boundary layer on the ground plane.

None of these studies, however, with perhaps the exception of the numerical simulations by Krajnović (2011), have extensively addressed the role, influence, and structure of the flow above the free-end surface, how this flow field relates to what is happening in the near-wake region, and how this local flow field is influenced by various parameters such as Reynolds number, aspect ratio, and the boundary layer thickness. In studies of the convective heat transfer from finite cylinders, Sparrow and Samie (1981) found different Reynolds number sensitivities for the heat transfer from the sides of the cylinder compared to the heat transfer from the free end. Their observation suggests that the parameters influencing the free-end flow pattern may be much different than those influencing the rest of the flow field, and study of the free-end flow field therefore warrants further attention. As a step towards better understanding the free-end flow field, this paper presents a literature review that summarizes the current understanding of the flow above the free end of a surface-mounted finite circular cylinder, focusing on experimental and numerical studies involving models of the flow field, surface oil flow visualization, pressure and heat flux distributions, velocity fields, and streamline patterns.

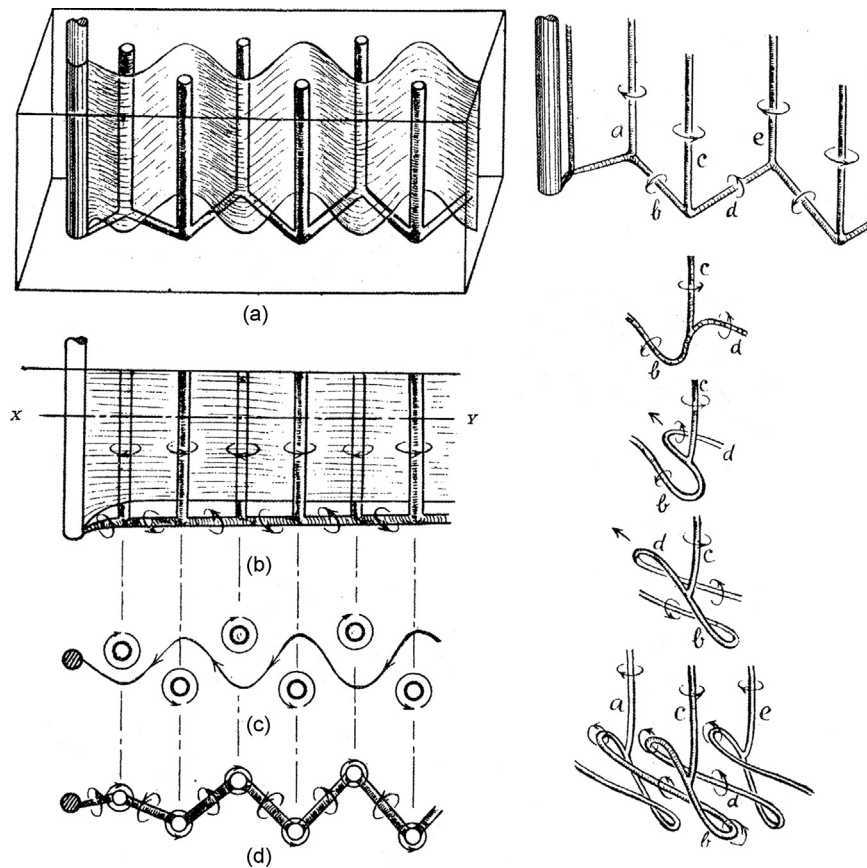


Fig. 2. Schematics of the wake vortex flow patterns for a finite circular cylinder (left) and the vortex deformation process (right) (from Taneda, 1952), based on flow visualization experiments at $Re=39-75$.

2. Models of the flow field

Several models of the flow field for surface-mounted finite-height circular cylinders and square prisms have been advanced in the literature, most of which have focused on the near-wake region and the vortex shedding. Many models have two descriptions, one for cylinders which are lower than the critical aspect ratio and one for cylinders which are greater than the critical aspect ratio. Few of these models, except perhaps for those based on the flow over low-aspect-ratio cylinders, have focused strongly on the flow patterns associated with the free end, how this local flow field relates to the flow in the near-wake region, and how it may be influenced by the cylinder's aspect ratio, the relative thickness of the boundary layer on the ground plane (δ/D or δ/H), the Reynolds number, and other parameters and flow conditions. It is noted that the majority of the experiments in the literature have been performed at $Re \approx 10^4-10^5$.

Perhaps the earliest model for the flow around the finite cylinder is based on the wake flow visualization experiments of Taneda (1952) at $Re=39-75$, who proposed the intricate vortex street structure shown in Fig. 2. Notable in this model is the effect of downwash that reduces the vertical extent of the wake, the interconnection of the Kármán vortex axes back to the cylinder free end, and the deformation of the vortices. However, the model did not explain the details of the vortex dynamics close to the cylinder, the origin of the trailing vortex interconnecting the Kármán vortices, nor examine the flow close to the free end.

Another early model for the flow around a surface-mounted finite-height circular cylinder was proposed by Etzold and Fiedler (1976) based on wind tunnel experiments at $Re=3 \times 10^4$. Their model (Fig. 3) shows the pair of streamwise tip vortex structures originating from the circumferential leading edge of the free end, and also the presence of a weaker streamwise vortex pair lower in the wake (the base vortex pair later characterized by Tanaka and Murata (1999) and Sumner et al. (2004)).

Kawamura et al. (1984a) proposed two models for the flow field, shown in Fig. 4, for cylinders either above or below the critical aspect ratio. Their models were based on wind tunnel measurements and oil-flow visualization experiments at $Re=3.2 \times 10^4$ and smoke flow visualization experiments at $Re=1.07 \times 10^4$. In their model for cylinders with aspect ratios larger than the critical value, Kármán vortex shedding occurs from the sides of the cylinder (Fig. 4(a)); below the critical aspect ratio, Kármán vortex shedding is absent. In terms of the flow over the free end, the schematics of Kawamura et al. (1984a) show the tip vortices originating from the circumferential leading edge of the free end, similar to Etzold and Fiedler (1976) (Fig. 3).

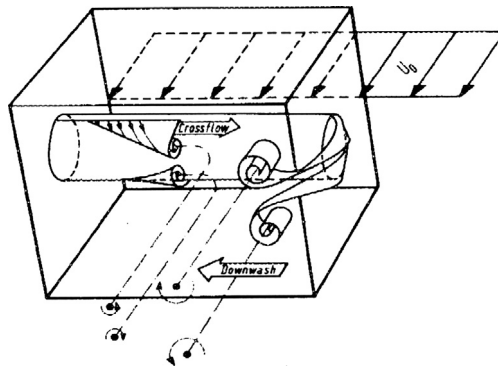


Fig. 3. Schematic of the flow around a finite circular cylinder (from Etzold and Fiedler (1976), based on wind tunnel experiments at $Re = 3 \times 10^4$), where U_0 is the freestream velocity.

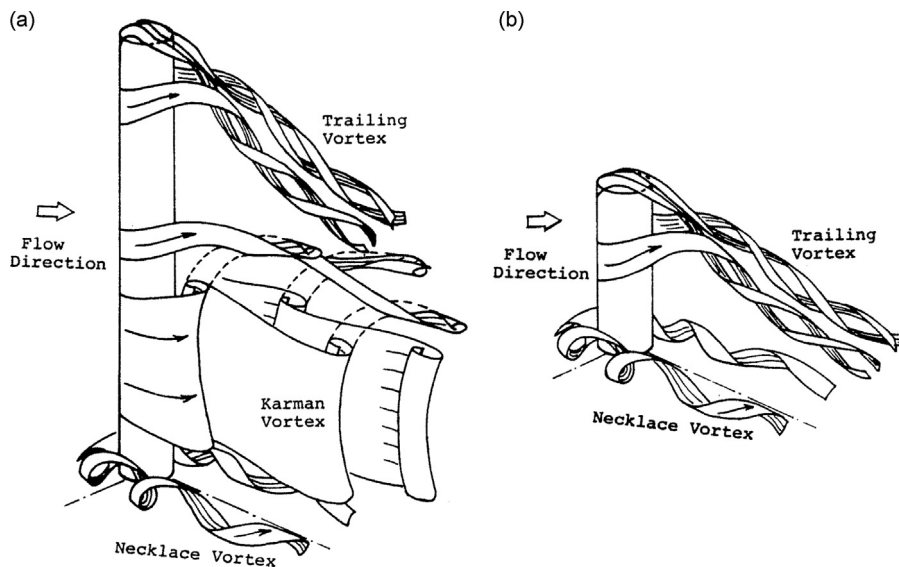


Fig. 4. Models of the flow field for surface-mounted finite-height circular cylinders proposed by Kawamura et al. (1984a), based on wind tunnel measurements and oil-flow visualization experiments at $Re = 3.2 \times 10^4$ and smoke flow visualization experiments at $Re = 1.07 \times 10^4$: (a) for aspect ratios greater than the critical aspect ratio; (b) for aspect ratios less than the critical aspect ratio.

In a second study, Kawamura et al. (1984b) presented a model applicable to higher-aspect-ratio cylinders but showed details of the flow about the free end (Fig. 5). Similar experimental techniques and Reynolds numbers were used as in Kawamura et al. (1984a). A prominent mean recirculation zone is featured on the free-end surface, including its reattachment line on the latter half of the surface. The figure shows the two ends of a “mushroom vortex” structure (and its sense of rotation) on either side of the free end. Its axis bends to become a prominent cross-stream vortex within the mean recirculation zone. In contrast to their models in Fig. 4, the streamwise trailing vortices in Fig. 5 are shown to originate from either side of the rear surface of the cylinder. Other prominent features include the bending downstream of the separation lines on the sides of the cylinder near the free end, which has been documented in many studies for both small and large aspect ratios (e.g., Gould et al., 1968; Okamoto and Yagita, 1973; Majumdar and Rodi, 1989; Fox et al., 1993; Pattenden et al., 2005; Rödiger et al., 2007; Tsutsui, 2012).

Agui and Andreopoulos (1992) presented a simple flow schematic, reproduced here in Fig. 6, which focused mostly on the horseshoe (or necklace) vortex structures upstream (which was the main emphasis of their study). Consequently, the flow features in the near wake are not well characterized. Their flow visualization experiments were conducted at $Re = 1.0 \times 10^5$ and 2.2×10^5 .

Hölscher and Niemann (1996) presented a detailed schematic of the finite-cylinder flow field applicable to low-aspect-ratio cylinders (Fig. 7) for the case of a thick turbulent (simulated atmospheric) boundary layer on the ground plane (their work did not specify a Reynolds number range, but is presumably applicable to $Re \approx 10^4$ – 10^6). Their schematic shows the bending of separation lines on the sides of the cylinder, the mean recirculation zone on the free-end surface containing the prominent cross-stream (mushroom) vortex, and the reattachment line on the free end. In contrast to the model of Kawamura et al. (1984b) in Fig. 5, the streamwise tip vortices are shown to originate from the sides of cylinder on the

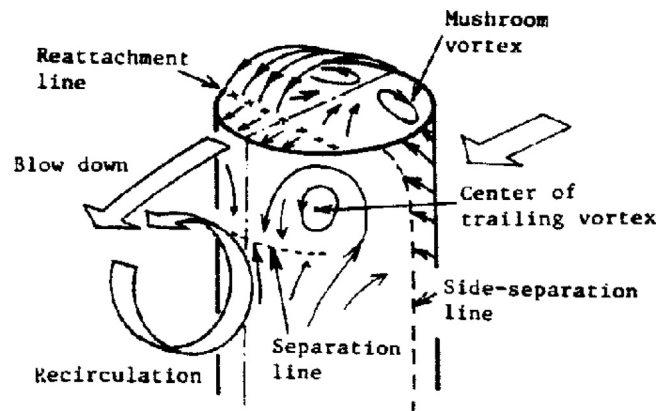


Fig. 5. Schematic of the local flow field for a high-aspect-ratio, surface-mounted finite-height circular cylinder (from Kawamura et al., 1984b), based on wind tunnel measurements and oil-flow visualization experiments at $Re=3.2 \times 10^4$ and smoke flow visualization experiments at $Re=1.07 \times 10^4$.

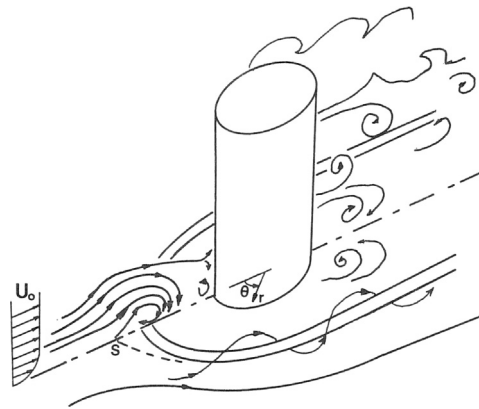


Fig. 6. Schematic of the flow field for a surface-mounted finite-height circular cylinder shown in Agui and Andreopoulos (1992), where S denotes the separation point on the ground plane upstream of the cylinder, and U_0 is the freestream velocity. Their schematic is associated with flow visualization experiments conducted at $Re=1.0 \times 10^5$ and 2.2×10^5 .

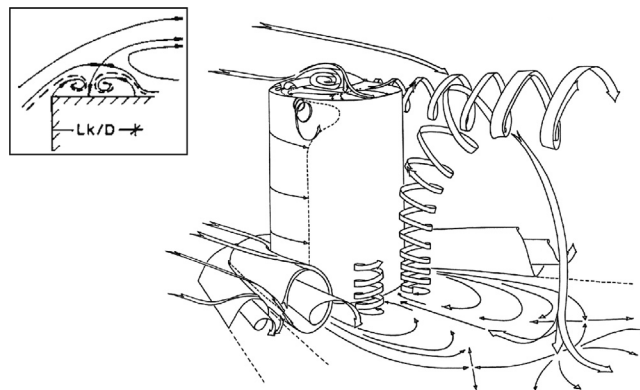


Fig. 7. Schematic of the local flow field for a low-aspect-ratio, surface-mounted finite-height circular cylinder in a thick turbulent (simulated atmospheric) boundary layer (from Hölischer and Niemann (1996)); a Reynolds number range is not specified, but is presumably applicable to $Re \approx 10^4$ – 10^6 . Enlargement shown of the region near the leading edge (from Palau-Salvador et al. (2010) and attributed to Hölischer), showing a pair of cross-stream vortices in this separation bubble region.

circumferential edge of the free end. Other small cross-stream vortex structures can be identified near the leading edge of the free-end surface. These small vortices are shown more clearly in the enlargement taken from the later work by Palau-Salvador et al. (2010) but attributed to Hölischer.

Johnston and Wilson (1996) also presented a model for the main streamwise tip vortex pair, shown in Fig. 8, and suggested that it results from the bending of the Kármán vortex axes towards the free end. Their model was supported by

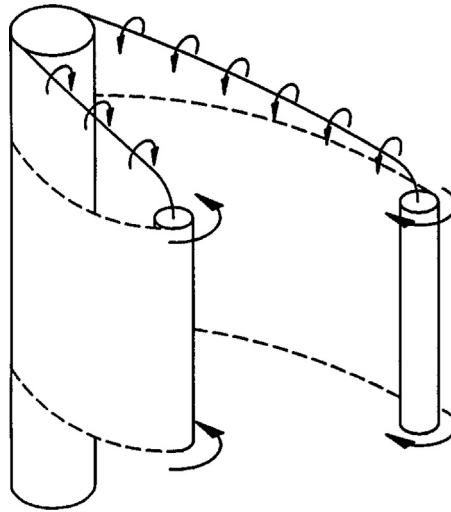


Fig. 8. Tip vortex model proposed by Johnston and Wilson (1996) for a finite-height circular cylinder (supported by flow visualization experiments at $Re=1800$).

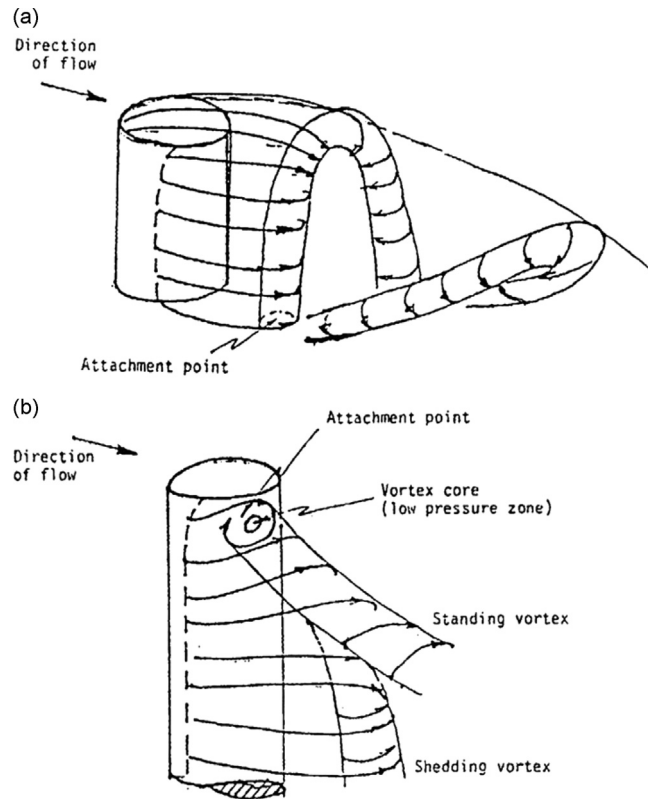


Fig. 9. Models of the flow field for a surface-mounted finite-height circular cylinder from Lee (1997), based on experiments conducted at $Re=3 \times 10^3$ – 1.5×10^4 for $AR=1$ – 15 , for (a) low-aspect-ratio cylinders, below the critical aspect ratio, and (b) cylinders greater than the critical aspect ratio.

flow visualization experiments at $Re=1800$. Their schematic shows the tip vortices connecting to the sides of the free-end surface, similar to Hölscher and Niemann (1996) (Fig. 7).

Two models were given by Lee (1997) for low and high aspect ratios (Fig. 9) based on experiments conducted at $Re=3 \times 10^3$ – 1.5×10^4 for $AR=1$ – 15 . Both models show the rearward bending of the boundary layer separation line on the side of the cylinder close to the free end. The model for low-aspect-ratio cylinders (Fig. 9(a)), those below the critical aspect ratio, showed “arch vortex” formation in the near-wake region (following the terminology of Taniguchi et al. (1981) and

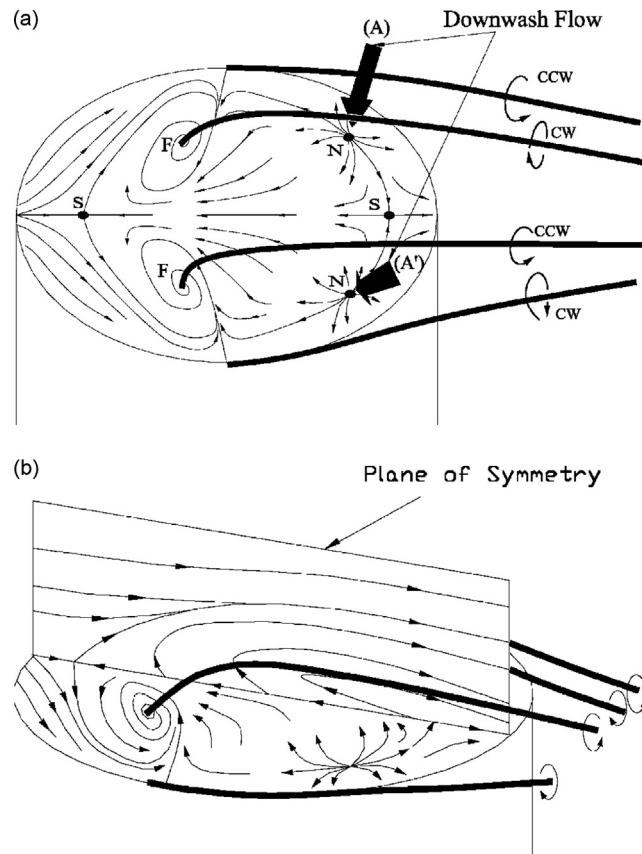


Fig. 10. Local flow field for a low-aspect-ratio, surface-mounted finite-height circular cylinder, from Roh and Park (2001, 2003): (a) surface topology; (b) schematic of flow field. The model is based on experiments conducted at $Re=5.92 \times 10^3$ and 1.48×10^5 .

Okamoto and Sunabashiri (1992)). In this model, flow separating from the circumferential leading edge of the free-end surface does not reattach but becomes contiguous with the arch vortex forming behind the cylinder. For high-aspect-ratio cylinders (Fig. 9(b)), above the critical aspect ratio, Kármán vortex shedding occurs from the sides of the cylinder and streamwise tip vortices (“standing” vortices) are shown to originate from the sides of the rear surface of the cylinder; this is similar to the second model of Kawamura et al. (1984b) in Fig. 5.

Roh and Park (2001, 2003) proposed a model of the free-end flow field (Fig. 10) which differs topologically from many of the other models in the literature. Their model was based on experiments that were conducted at $Re=5.92 \times 10^3$ and 1.48×10^5 . This model, with the identification of two nodes on the free-end surface (Fig. 10(a)), and two pairs of streamwise trailing vortices (Fig. 10(a,b)), has not been supported by many other experimental or numerical studies, as discussed by Pattenden et al. (2005) and Krajnović (2011). Furthermore, the schematic in Fig. 10(b) does not seem to indicate reattachment on the free-end surface. Rather than showing the mushroom vortex connecting across the symmetry plane to the two foci, the foci are depicted as the origins of a second pair of streamwise vortices, known as the “tornado-like vortices”. The other pair, the “side tip vortices”, originates from the sides of the free-end surface similar to the schematic of Hölscher and Niemann (1996) (Fig. 7). Only the surface oil film visualization results of Rödiger et al. (2007) for a cylinder of $AR=2$ (see ahead to Fig. 16(n)), and the large eddy simulations (LES) of Palau-Salvador et al. (2010) for cylinders of $AR=2.5$ and 5 (see ahead to Figs. 25 and 26), somewhat support the topology of Roh and Park (2001, 2003) and the two nodes near the trailing edge.

The experiments of Sumner et al. (2004) at $Re=6 \times 10^4$ showed the existence of a second pair of time-averaged streamwise vortices, known as the “base vortices”, which appear in the lower part of the wake for cylinders greater than the critical aspect ratio. This supported earlier observations by Tanaka and Murata (1999). For cylinders less than the critical aspect ratio, the base vortex pair is absent. Their schematic of the flow field for cylinders above the critical aspect ratio (Fig. 11) illustrates the main vortex structures; however, their research did not address the flow field associated with the free end nor did they identify the origin of the streamwise vortex structures.

A schematic of the mean flow field from Pattenden et al. (2005, 2006) for low-aspect-ratio finite cylinders is shown in Fig. 12; this model of the flow field is based on their experiments (Pattenden et al., 2005) and numerical simulations (Pattenden et al., 2006) for a cylinder of $AR=1$ at $Re=2 \times 10^5$. In this schematic, the approaching flow separates from the circumferential leading edge of the cylinder's free end and a recirculation zone forms on the free-end surface. Recirculating

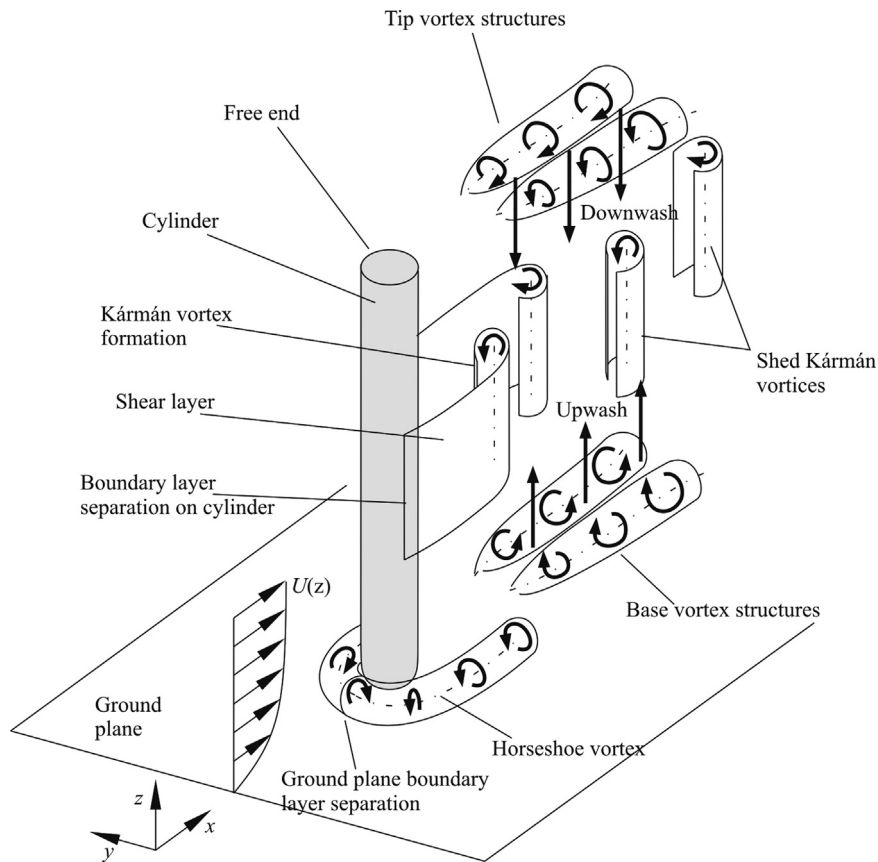


Fig. 11. Schematic of the flow field for finite circular cylinders greater than the critical aspect ratio based on the work by Sumner et al. (2004), as shown in Einian et al. (2010).

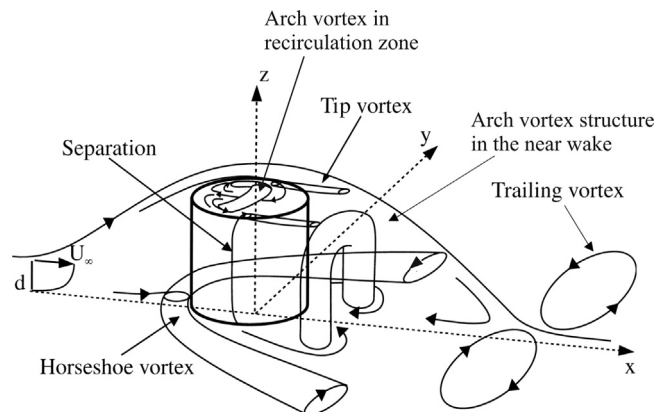


Fig. 12. Schematic of the local flow field for a low-aspect-ratio, surface-mounted, finite-height circular cylinder (from Pattenden et al. (2005, 2006)) (where d is the boundary layer thickness). Note that the coordinate system's origin is at the cylinder-wall junction. The sketch is based on experiments (Pattenden et al., 2005) and numerical simulations (Pattenden et al., 2006) for a cylinder of $AR=1$ at $Re=2 \times 10^5$.

streamlines are shown close to the surface, which illustrate reverse flow along the centerline of the free-end surface that divides near the leading edge and returns along the two sides. An “arch vortex” structure (the mushroom vortex of Kawamura et al. (1984a, 1984b) in Figs. 4 and 5) is located above the free-end surface within the mean recirculation zone; this arch vortex is distinct from the similarly named structure, also identified in Fig. 12, that is formed and shed in the near-wake region for finite cylinders of less than the critical aspect ratio (Fig. 8(a)) (e.g., Taniguchi et al. (1981)). The two ends of this arch vortex terminate on either side of the free-end surface, similar to the model of Kawamura et al. (1984b) in Fig. 5. In their model, tip vortices are seen to originate on either side of the free-end surface, similar to the schematics of Hölscher and Niemann (1996) (Fig. 7), Johnston and Wilson (1996) (Fig. 8), and Roh and Park (2001, 2003) (Fig. 10). However, in the

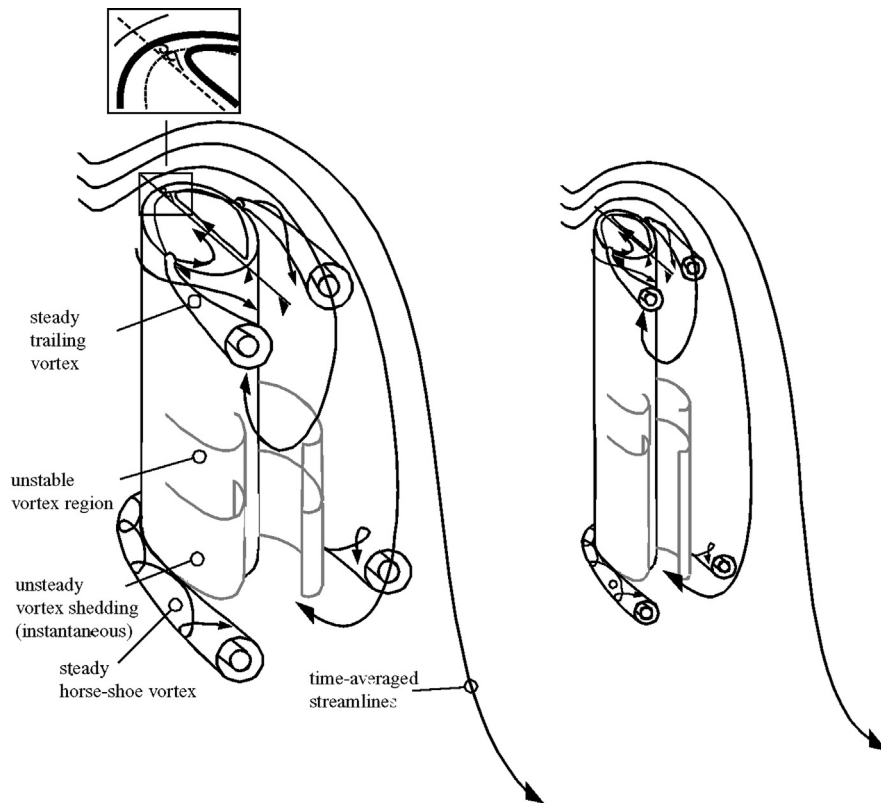


Fig. 13. Models of the flow around surface-mounted finite circular cylinders of $AR=2.5$ (left) and $AR=5$ (right) reported in [Donnert et al. \(2007\)](#), attributed to [Kappler \(2002\)](#). The model is based on experiments carried out at $Re=2.2 \times 10^4$ – 4.4×10^4 .

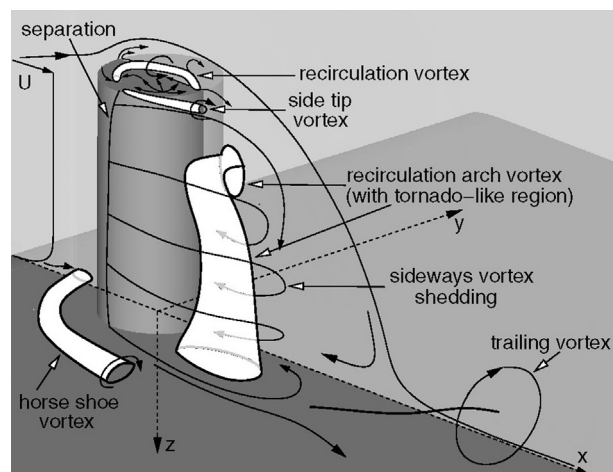


Fig. 14. Model of the flow field for a surface-mounted finite-height circular cylinder of $AR=2$, based on numerical simulations at $Re=2 \times 10^5$, from [Frederich et al. \(2007\)](#) (where U is the freestream velocity). Note the orientation of the coordinate system.

lower part of the wake, the model of [Pattenden et al. \(2005, 2006\)](#) (Fig. 12) shows another “trailing vortex” pair that is distinct from the tip vortices; a similar model was proposed by [Frederich et al. \(2007\)](#) described below.

Two models were also shown by [Donnert et al. \(2007\)](#) for $AR=2.5$ and 5 (Fig. 13) at $Re=2.2 \times 10^4$ to 4.4×10^4 which provided details of the near-wake region and the flow above the free end; these models were attributed to the earlier work of [Kappler \(2002\)](#). Their models show the mean recirculation zone above the free end, the reverse flow on the free-end surface, a pair of vortices localized near the leading edge of the free-end surface, and the tip vortices originating from the sides of the free-end surface. This origin for the trailing vortices is consistent with the models of [Hölscher and Niemann \(1996\)](#) (Fig. 7), [Roh and Park \(2001, 2003\)](#) (Fig. 10), and [Pattenden et al. \(2005, 2006\)](#) (Fig. 12). In terms of the free-end flow field, the only difference between the cases for $AR=2.5$ and $AR=5$ is the pair of vortices near the leading edge, which is

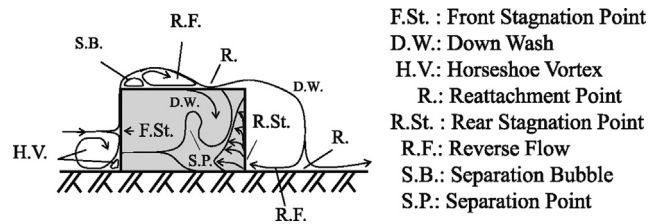


Fig. 15. Schematic of the local flow field for a low-aspect-ratio, surface-mounted finite-height circular cylinder (from Tsutsui and Kawahara, 2006 and Tsutsui, 2012); the model is based on experiments with very-low-aspect-ratio ($AR \leq 1$) finite cylinders at $Re = 1.1 \times 10^4$ – 1.1×10^5 .

absent in the model for $AR=5$. This vortex pair can also be seen in the schematic of Hölscher and Niemann (1996) in Fig. 7, as discussed in Palau-Salvador et al. (2010). Despite this difference in the models, Donnert et al. (2007) noted that the free-end flow field was not significantly influenced by AR compared to the central portion of the near wake.

Frederich et al. (2007) also proposed a model based on numerical simulations of the flow around a finite cylinder of $AR=2$ at $Re=2 \times 10^5$. This model, shown in Fig. 14, is one of the few models to include both the near-wake and the free-end flow fields. In this model, “side-tip vortices” (using the terminology of Roh and Park, 2001, 2003 (Fig. 10)) are generated from the sides of the free-end surface, similar to what is seen in the models of Hölscher and Niemann (1996) (Fig. 7), Roh and Park (2001, 2003) (Fig. 10), Pattenden et al. (2005, 2006) (Fig. 12), and Donnert et al. (2007) (Fig. 13). Frederich et al. (2007) described the side-tip vortices as local structures that are distinct from the streamwise “trailing” vortices seen in the other models by Kawamura et al. (1984a, 1984b) (Figs. 4 and 5) and Sumner et al. (2004) (Fig. 9). According to Frederich et al. (2007), these side-tip vortices “are merged into the recirculation region” whereas the trailing vortices shown in Fig. 14 arise downstream of the near-wake recirculation zone. In this respect, their model seems to exhibit some similarity to that of Pattenden et al. (2005, 2006), where a pair of larger trailing vortices is seen in the lower part of the near-wake region (Fig. 12).

Another schematic was given by Tsutsui and Kawahara (2006) and Tsutsui (2012) based on experiments with very-low-aspect-ratio ($AR \leq 1$) finite cylinders (Fig. 15) at $Re = 1.1 \times 10^4$ – 1.1×10^5 ; many of the flow features identified in Fig. 15 are commonly observed at higher AR also. A mean recirculation zone (denoted by “R.F.” or “Reverse Flow”) forms on the free end of the circular cylinder due to the reattachment (denoted by “R”) of the separated shear layer onto on the free-end surface. A clockwise cross-stream vortex, corresponding to the mushroom vortex of Kawamura et al. (1984a, 1984b) (Figs. 4 and 5), or the arch vortex of Pattenden et al. (2005, 2006) (Fig. 12), is seen within this recirculation zone. A small separation bubble (denoted by “S.B.”) is shown just downstream of the leading edge, which forms when the reverse flow close to the free-end surface separates as it approaches the leading edge. This feature was noticed by Sparrow and Samie (1981) as a “zone of weak forward flow”, and small cross-stream vortices and critical points associated with this bubble are depicted in various models (e.g., Hölscher and Niemann (1996) (Fig. 7), Donnert et al. (2007) (Fig. 13), Palau-Salvador et al. (2010), Krajnović (2011)). The notable difference in the schematic of Tsutsui and Kawahara (2006) and Tsutsui (2012) is the unusual shape of the side separation line near the free end (Fig. 15), which is unique to very-low-aspect-ratio ($AR \leq 1$) finite cylinders.

3. Surface oil flow visualization

Many of the flow field models and schematics shown in the previous figures were based extensively on surface oil flow visualization experiments and the mean flow topology revealed by the oil flow patterns. A selection of published images of the flow on the free-end surface is shown in Fig. 16, with the majority of the images for lower aspect ratios, $AR \leq 2$ (Fig. 16(a–n)).

At very low aspect ratios ($AR \leq 1$) the flow visualization images show the leading edge separation bubble (see the schematic of Tsutsui (2012), Fig. 15) just downstream of the leading edge; in Fig. 16(a–h) this is denoted by the white crescent-shaped region. The streamwise extent of this region seems to lengthen as the aspect ratio increases; for example, compare the size of this region for $AR=0.125$ (Fig. 16(a)), where it is almost nonexistent, to that of $AR=0.5$ (Fig. 16(g)) and $AR=1$ (Fig. 16(h)). The separation bubble can also be identified at higher aspect ratios, where the flow visualization images show the weak streamwise flow near the surface and the spreading of this flow towards the sides of the cylinder (Fig. 16(i,n)). The streamwise extent of the separation bubble on the centerline is marked by a separation saddle point (point “ST” in Fig. 16(i), or point “A” in Fig. 16(k)), as shown in the topology of Roh and Park (2001, 2003) (Fig. 10(a)); for the case shown in Fig. 16(i), this separation saddle point was located at $x/D \approx -0.4$ (Pattenden et al., 2005). Some studies, however, do not comment on the existence of this separation bubble, perhaps due to the limited resolution of the surface flow visualization method or other measurement technique. For instance, Pattenden et al. (2005) could not resolve the separation bubble flow pattern in their ensemble-averaged particle image velocimetry (PIV) velocity field measurements in the vertical symmetry plane above the free end, despite identifying the region in their surface oil flow visualization images. It is also possible that the appearance of the separation bubble depends on the flow conditions, including Re , AR , δ/D , and/or δ/H , but this has yet to be determined.

Also prominent in the flow visualization images is the reattachment line, which divides the recirculating/reversing flow upstream from the attached/forward-moving flow downstream (Sparrow and Samie, 1981); this reattachment line is shown

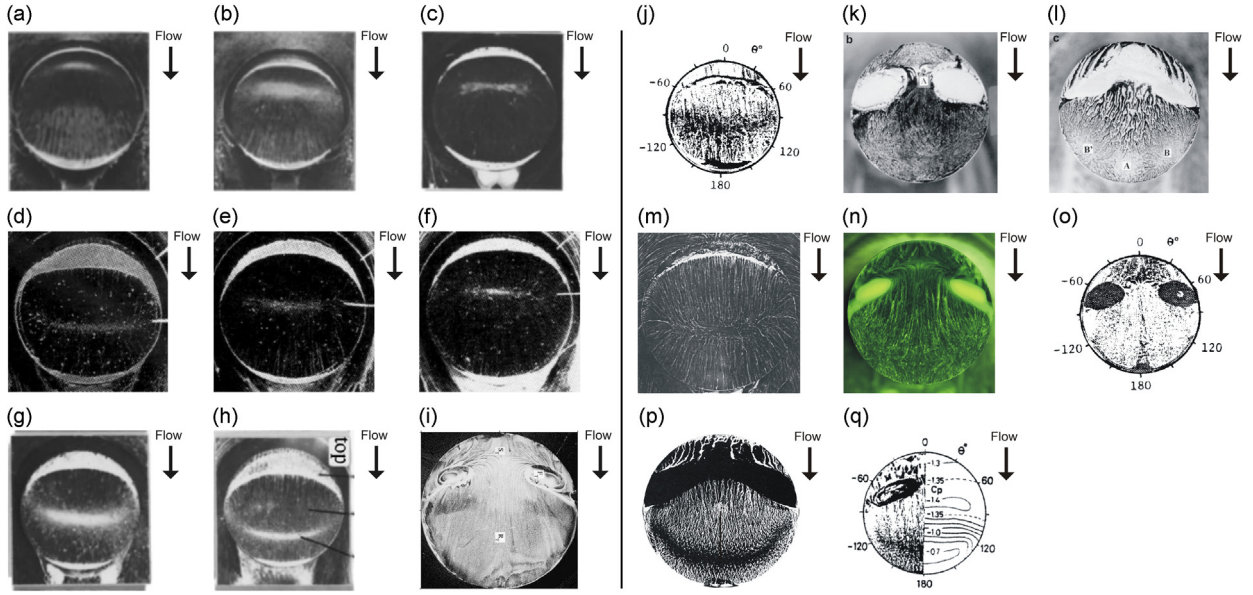


Fig. 16. Surface oil flow visualization results for the flow over the free end of a surface-mounted finite-height circular cylinder: (a) $AR=0.125$, $Re=1.1 \times 10^5$, $\delta/D=0.65$, $\delta/H=5.2$, Tsutsui and Kawahara (2006), (b) $AR=0.1875$, $Re=1.1 \times 10^5$, $\delta/D=0.65$, $\delta/H=3.47$, Tsutsui and Kawahara (2006), (c) $AR=0.25$, $Re=1.1 \times 10^5$, $\delta/D=0.65$, $\delta/H=2.6$, Tsutsui and Kawahara (2006), (d) $AR=0.35$, $Re=8.4 \times 10^4$, $\delta/D=0.032$, $\delta/H=0.09$, Tsutsui et al. (2000), (e) $AR=0.35$, $Re=8.4 \times 10^4$, $\delta/D=0.207$, $\delta/H=0.09$, Tsutsui et al. (2000), (f) $AR=0.35$, $Re=8.4 \times 10^4$, $\delta/D=0.406$, $\delta/H=1.16$, Tsutsui et al. (2000), (g) $AR=0.5$, $Re=1.1 \times 10^5$, $\delta/D=0.65$, $\delta/H=1.3$ Tsutsui and Kawahara (2006), (h) $AR=1$, $Re=1.1 \times 10^5$, $\delta/D=0.65$, $\delta/H=0.65$, Tsutsui and Kawahara (2006), (i) $AR=1$, $Re=2 \times 10^5$, $\delta/D=0.1$, $\delta/H=0.1$, Pattenden et al., 2005, (j) $AR=1$, $Re=3.2 \times 10^4$, $\delta/D=1$, $\delta/H=1$, Hiwada et al., 1984, (k) $AR=1.25$, $Re=1.48 \times 10^5$, $\delta/D=0.0625$, $\delta/H=0.05$, Roh and Park (2003), (l) $AR=1.25$, $Re=1.48 \times 10^5$, $\delta/D=0.0625$, $\delta/H=0.05$, Roh and Park (2003), (m) $AR=1.9$, $Re=5 \times 10^5$, $\delta/D=3.8$, $\delta/H=2$, Majumdar and Rodi (1989), (n) $AR=2$, $Re=2 \times 10^5$, $\delta/D=0.184$, $\delta/H=0.092$, Rodiger et al. (2007), (o) $AR=4$, $Re=3.2 \times 10^4$, $\delta/D=1$, $\delta/H=0.25$, Hiwada et al., 1984, (p) $AR=7$, $Re=2.5 \times 10^4$, δ/D and δ/H not given Sparrow and Samie (1981), (q) $AR=8$, $Re=3.2 \times 10^4$, $\delta/D=1$, $\delta/H=0.125$, Kawamura et al. (1984a).

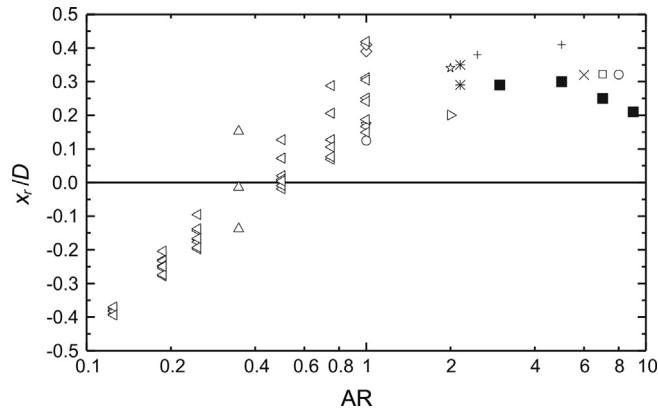


Fig. 17. Location of the reattachment saddle point on the centerline of the free-end surface, for surface-mounted finite-height circular cylinders: \square , Sparrow and Samie (1981); \circ , Kawamura et al. (1984a, 1984b); Δ , Tsutsui et al. (2000); ψ , Leder (2003); ∇ , Pattenden et al. (2005); \lessdot , Pattenden et al. (2006); \lessdot , Tsutsui and Kawahara (2006); \square , Hain et al. (2008); \gt , Dobriloff and Nitsche (2009); $+$, Palau-Salvador et al. (2010); \times , Krajnović (2011); \blacksquare , Rostamy et al. (2012).

prominently in the schematics of Kawamura et al. (1984b) (Fig. 5), Hölscher and Niemann (1996) (Fig. 7) and Tsutsui (2012) (Fig. 15). On the centerline, the reattachment position is denoted by a reattachment saddle point (point “RT” in Fig. 16(i), or point “A” in Fig. 16(l)). At very low aspect ratios, the reattachment line seems to be straight (Fig. 16(a–f) for $AR=0.125$ – 0.35 , and as depicted by Kawamura et al. (1984b) for higher AR (Fig. 5)). At higher aspect ratios, the line attains a curved (or “crescent”) shape, with reattachment occurring earlier near the outer edges of the free end (e.g., Fig. 16(g, h, j, p, q) for $AR=0.5$ – 8). In the flow visualization images from Tsutsui et al. (2000) and Tsutsui and Kawahara (2006) the reattachment line appears as a prominent white band on the free-end surface (Fig. 16(a–h)). In the other flow visualization images it is more difficult to discern (highlighting the importance of high-quality flow visualization techniques and the need for careful interpretation) with the possible exception of Fig. 16(p), but can be approximated by the location of a wide band or a change in the shape and orientation of the dye streak lines.

The mean reattachment line position on the centerline (x_R/D , the location of the reattachment saddle point) as a function of AR is shown in Fig. 17. This compilation of published data shows a general tendency, at least for lower aspect ratios, for the reattachment position to move downstream as AR increases. For example, compare the position of the line in the flow visualization images as AR changes from AR=0.125 (Fig. 16(a)) to AR=1 (Fig. 16(h)). Unfortunately, there are limited data for higher aspect ratios from which to interpret the trend (see Fig. 17). The location of the reattachment line is also sensitive to the relative boundary layer thickness (δ/H) on the ground plane: as δ/H increases, the reattachment line moves upstream closer to the leading edge (Tsutsui et al., 2000; Tsutsui, 2012); for example, compare the position of the line for AR=0.35 as δ/H changes from $\delta/H=0.032$ (Fig. 16(d)) to $\delta/H=0.207$ (Fig. 16(e)) and to $\delta/H=0.406$ (Fig. 16(f)). Physical explanations for these behaviors, with changes in AR and boundary layer thickness, are generally lacking in the literature.

Another flow feature of interest is the pair of foci, one focus on either side of the centerline (points “FT” in Fig. 16(i), and shown in the model of Kawamura et al. (1984b) (Fig. 5)). In most models, the foci represent the terminal points of the arch (or mushroom) vortex that occupies the mean recirculation zone. In the case of Roh and Park (2001, 2003), their model (Fig. 10) stands in contrast to nearly all of the other studies in the literature. Their model suggests the foci are the origins of “tornado-like” vortices that extend into the near wake. From the flow visualization images in Fig. 16, whether foci are observed or not seems to be related both to AR and δ/H , although the resolution of the visualization results may also play a factor. For very low aspect ratios, AR < 1 (Fig. 16(a–g)), none of the flow visualization images show evidence of foci over a wide range of δ/H , ranging from $\delta/H=0.09$ (Fig. 16(d)) to $\delta/H=5.2$ (Fig. 16(a)). For AR=1 (Fig. 16(h–j)), the appearance of the foci depends on the boundary layer thickness: as the boundary layer thickness increases and surpasses the height of the cylinder, the foci disappear. For example, foci are seen clearly when $\delta/H=0.1$ (Fig. 16(i)) but are absent when $\delta/H=0.65$ (Fig. 16(h)) and $\delta/H=1$ (Fig. 16(j)). At higher aspect ratios, foci are seen in all the flow visualization images but one: for AR=1.9 and $\delta/H=2$ (Fig. 16(m)) there are no discernible foci, suggesting that very thick boundary layers may suppress their formation and the formation of the arch (mushroom) vortex. This result remains to be verified in experiments or simulations, however.

The model of Roh and Park (2001, 2003) shown in Fig. 10 also shows two nodes on the free-end surface near the trailing edge on either side of the centerline. These are seen in their flow visualization image in Fig. 16(l) as points “B” and “B’”. Rödiger et al. (2007) suggest that nodes can be seen in their flow visualization results also (Fig. 16(n)). Furthermore, nodes can also be discerned in the numerical simulations of Palau-Salvador et al. (2010) and Krajnović (2011) (see ahead to Figs. 25 and 27(b)).

4. Pressure distribution

Measurements of the mean static pressure distribution on the free-end surface have been reported in several studies for various aspect ratios and boundary layer thicknesses, with the dominant influencing parameter being the aspect ratio (Hiwada et al., 1984; Kawamura et al., 1984a; Majumdar and Rodi, 1989; Tsutsui et al., 2000; Rödiger et al., 2007; Dobriloff and Nitsche, 2009; Iungo et al., 2012; Tsutsui, 2012). A selection of data, illustrated using contours of the dimensionless pressure coefficient, C_p , is shown in Fig. 18. For all aspect ratios, the pressure over the entire free-end surface is negative. The lowest (most negative) pressures are experienced close to the leading edge and beneath the mean recirculation zone up until the reattachment line. For very-low-aspect-ratio cylinders, AR ≤ 1, the point of most negative pressure is located at the interface between the separation bubble and the region of reverse flow (Tsutsui, 2012); this pressure becomes more negative as the aspect ratio increases. The smallest (most negative) values of C_p are reported for the higher-aspect-ratio cylinders of AR=1.9 (with $C_p=-1.2$, Fig. 18(k)) and AR=8 (with $C_p=-1.4$, Fig. 18(o)).

For a cylinder of AR=2, Rödiger et al. (2007) noticed that the minimum pressure occurs centrally between the two foci; this is consistent with the results of Hiwada et al. (1984) and Kawamura et al. (1984a) shown in Fig. 18(n,o). Higher (less negative) pressures are experienced around the reattachment line and towards the trailing edge. Within this region the mean pressures also tend to be more uniform or slowly varying (Tsutsui et al., 2000). However, as noted by Rödiger et al. (2007) for AR=2, this is also a region of higher pressure fluctuations compared to the flow beneath the mean recirculation zone (see ahead to Fig. 19(m), where the pressure fluctuation contours are presented alongside heat flux fluctuations). Higher pressure fluctuations were also seen in this region by Dobriloff and Nitsche (2009) for AR=2.

The mean pressure measurements by Dobriloff and Nitsche (2009) for AR=2 (Fig. 18(l)) and Hiwada et al. (1984) for AR=4 (Fig. 18(n)) are perhaps the only ones to show the presence of the foci; this level of detail is not resolved in the other examples shown in Fig. 18. The foci are identified by two localized regions of lower pressure on the surface.

Phase-averaged surface pressure measurements by Dobriloff and Nitsche (2009) show little variation in the pressure distribution on the free-end surface, including the low-pressure regions about the foci. This important result suggests that the flow over the free end, including the arch (or mushroom) vortex, may not be strongly periodic compared to what occurs in the near-wake region. This lack of (or weak) periodicity for the free-end flow field was also reported by Iungo et al. (2012) for surface pressure fluctuations on the free end of a cylinder of AR=3 ($Re=1 \times 10^5$, $\delta/H=0.09$). They noted the absence of the vortex shedding signal in the pressure measurements made on the free end, in contrast to pressure measurements made on the side surfaces of the cylinder. Instead, they reported a weaker and more irregular low-frequency component within the free-end pressure measurements (corresponding to $St \approx 0.07-0.08$). Similar low-frequencies near the free end have been found in other finite-cylinder studies, including Kitagawa et al. (1999, 2002) and Park and Lee (2000, 2002, 2004). Kitagawa et al. (1999, 2002) attributed the low frequency signal to “tip-associated vortex shedding” with no alternating type behavior.

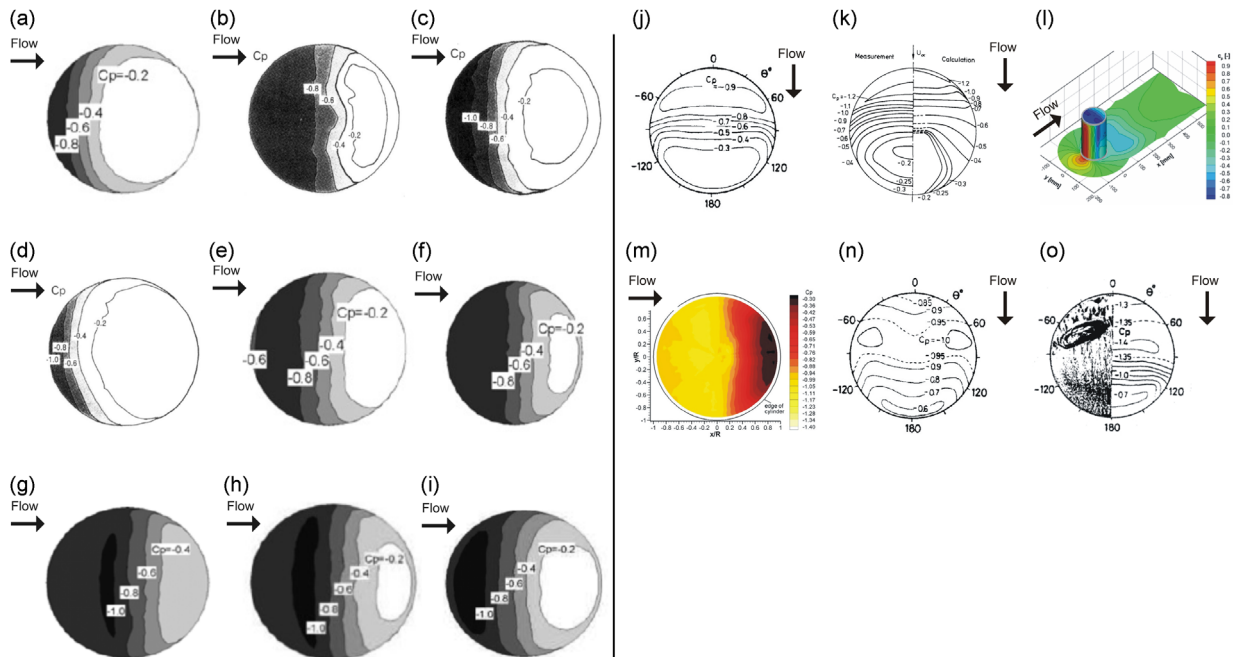


Fig. 18. Mean surface static pressure distributions (contours of the mean pressure coefficient, C_p) for the flow over the free end of a surface-mounted finite-height circular cylinder. (a) $AR=0.25$, $Re=1.1 \times 10^5$, $\delta/D=0.65$, $\delta/H=2.6$, [Tsutsui \(2012\)](#), (b) $AR=0.35$, $Re=8.4 \times 10^4$, $\delta/D=0.032$, $\delta/H=0.09$, [Tsutsui et al. \(2000\)](#), (c) $AR=0.35$, $Re=8.4 \times 10^4$, $\delta/D=0.207$, $\delta/H=0.59$, [Tsutsui et al. \(2000\)](#), (d) $AR=0.35$, $Re=8.4 \times 10^4$, $\delta/D=0.406$, $\delta/H=1.16$, [Tsutsui et al. \(2000\)](#), (e) $AR=0.5$, $Re=1.1 \times 10^5$, $\delta/D=0.65$, $\delta/H=1.3$, [Tsutsui \(2012\)](#), (f) $AR=0.75$, $Re=1.1 \times 10^5$, $\delta/D=0.65$, $\delta/H=0.87$, [Tsutsui \(2012\)](#), (g) $AR=1$, $Re=1.1 \times 10^5$, $\delta/D=0.325$, $\delta/H=0.325$, [Tsutsui \(2012\)](#), (h) $AR=1$, $Re=1.1 \times 10^5$, $\delta/D=0.65$, $\delta/H=0.65$, [Tsutsui \(2012\)](#), (i) $AR=1$, $Re=1.1 \times 10^5$, $\delta/D=1.5$, $\delta/H=1.5$, [Tsutsui \(2012\)](#), (j) $AR=1$, $Re=3.2 \times 10^4$, $\delta/D=1$, $\delta/H=1$, [Hiwada et al. 1984](#), (k) $AR=1.9$, $Re=5 \times 10^5$, $\delta/D=3.8$, $\delta/H=2$, [Majumdar and Rodi \(1989\)](#), (l) $AR=2$, $Re=2 \times 10^5$, δ/D and δ/H not given [Dobriloff and Nitsche \(2009\)](#), (m) $AR=2$, $Re=2 \times 10^5$, $\delta/D=0.184$, $\delta/H=0.092$, [Rodriguez et al. \(2007\)](#), (n) $AR=4$, $Re=3.2 \times 10^4$, $\delta/D=1$, $\delta/H=0.25$, [Hiwada et al. 1984](#), (o) $AR=8$, $Re=3.2 \times 10^4$, $\delta/D=1$, $\delta/H=0.125$, [Kawamura et al. \(1984a\)](#).

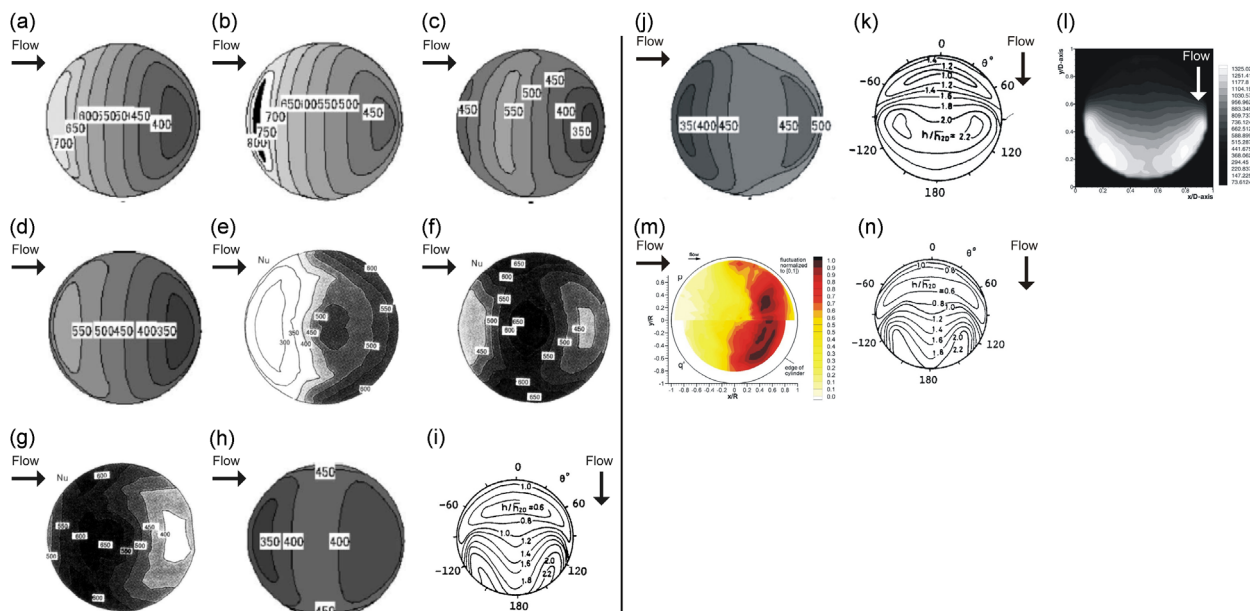


Fig. 19. Heat and mass transfer distributions on the free end of a surface-mounted finite-height circular cylinder: Nu = mean Nusselt number; Sh = mean Sherwood number; $h/h_{1/20}$ = mean heat flux normalized against the mean heat flux for a two-dimensional (infinite) cylinder; q'' = normalized heat flux fluctuations. (a) AR = 0.125, Re = 1.1×10^5 , $\delta/D = 0.65$, $\delta/H = 5.2$, Tsutsui and Kawahara (2006), (b) AR = 0.1875, Re = 1.1×10^5 , $\delta/D = 0.65$, $\delta/H = 3.47$, Tsutsui and Kawahara (2006), (c) AR = 0.25, Re = 1.1×10^5 , $\delta/D = 0.325$, $\delta/H = 1.3$, Tsutsui and Kawahara (2006), (d) AR = 0.25, Re = 1.1×10^5 , $\delta/D = 0.65$, $\delta/H = 2.6$, Tsutsui and Kawahara (2006), (e) AR = 0.35, Re = 8.4×10^4 , $\delta/D = 0.032$, $\delta/H = 0.09$, Tsutsui et al. (2000), (f) AR = 0.35, Re = 8.4×10^4 , $\delta/D = 0.207$, $\delta/H = 0.59$, Tsutsui et al. (2000), (g) AR = 0.35, Re = 8.4×10^4 , $\delta/D = 0.406$, $\delta/H = 1.16$, Tsutsui et al. (2000), (h) AR = 0.5, Re = 1.1×10^5 , $\delta/D = 0.65$, $\delta/H = 1.3$, Tsutsui and Kawahara (2006), (i) AR = 1, Re = 3.2×10^4 , $\delta/D = 0.1$, $\delta/H = 0.1$, Kawamura et al. (1984c).

Park and Lee (2000, 2002, 2004) reported a low-frequency component in the upper part of the wake on the wake centerline ($z/H=0.95$, for $x/D=0.6$ to 2.4 , $y/D=0$, $Re=2 \times 10^4$), and also away from the wake centerline (up to $x/D=6$ at $y/D=-2$ in some cases), that was independent of the cylinder aspect ratio and the vortex shedding frequency (for $AR=6, 10, 13$). Similar to Kitagawa et al. (1999, 2002), their measurements at $y/D=\pm 2$ indicated the low frequency had no associated phase difference across the wake and was therefore not associated with alternate vortex shedding. They attributed this low frequency to a periodicity of the tip vortex pair.

An increase in the relative thickness of the boundary layer tends to increase the size of the higher-pressure (less negative) region on the downstream portion of the free end, mirroring the behavior of the reattachment line which moves upstream with increasing δ/H (Tsutsui et al., 2000; Tsutsui, 2012). This can be seen in the pressure data for $AR=0.35$ as δ/H increases from $\delta/H=0.09$ (Fig. 18(b)), to $\delta/H=0.59$ (Fig. 18(c)), and to $\delta/H=1.16$ (Fig. 18(d)). A similar trend is seen for the cylinders of $AR=1$ (Fig. 18(g–j)).

5. Heat and mass transfer

Several studies report surface heat and mass transfer measurements on the free-end surface of a finite circular cylinder (Sparrow and Samie, 1981; Kawamura et al., 1984c; Tsutsui et al., 2000; Roh and Park, 2001; Tsutsui and Kawahara, 2006; Rödiger et al., 2007). The results resemble the oil flow visualization patterns and pressure distributions described above. Selected results for a range of aspect ratios and relative boundary layer thicknesses are shown in Fig. 19. The region of highest heat transfer is where the flow reattaches onto the free-end surface and towards the trailing edge, and the lowest heat transfer occurs in the region of reverse flow beneath the mean recirculation zone and in the vicinity of the separation bubble just after of the leading edge (Tsutsui et al., 2000; Tsutsui and Kawahara, 2006); these trends can be seen in most of the results in Fig. 19, for $AR \geq 0.25$. The main exception is for very low aspect ratios, where the highest heat transfer occurs just downstream of the leading edge ($AR=0.125$ and 0.1875 , Fig. 19(a,b)).

As the boundary layer thickness increases, the region of highest heat transfer shifts upstream similar to what is observed for the location of the reattachment line (Tsutsui et al., 2000); see Fig. 19(e,f,g) for $AR=0.35$. For thin boundary layers ($\delta/H < 1$), the heat transfer characteristics on the free end are not overly sensitive to changes in aspect ratio (Kawamura et al., 1984c); a comparison of the results for $AR=1$ (Fig. 19(i)) and $AR=6$ (Fig. 19(n)) shows similar heat flux contours. In contrast, with a thick boundary layer ($\delta/H=1$) the contours are much different; compare Fig. 19(i) and (k) for $AR=1$, which show the higher heat transfer region shifting upstream and intensifying with the thicker boundary layer. Whether these boundary layer effects are also found for higher aspect ratios has not been explored.

Measurements of the mass transfer on the free end of a cylinder of $AR=1.25$ (Fig. 19(l)), by Roh and Park (2001) show strong reduction in the local mean Sherwood number on the front part of the cylinder in the vicinity of the separation bubble and arch vortex and beneath the mean recirculation zone. The lower mass transfer in this region was attributed to the more complex near-surface flow field involving the foci, the separation saddle point, and the lower flow velocities. They noted that the mass transfer on the downstream half of the free-end surface was nearly twice as high as that on the upstream half.

Measurements of the heat flux fluctuations on the free end of a cylinder of $AR=2$, by Rödiger et al. (2007), showed that the highest fluctuations occur on the rear half of the free-end surface where the separated flow has reattached.

6. Flow field and velocity field

The flow field above the free end has been examined in several studies using flow visualization, velocity measurements, and numerical simulations. Some of the main studies that have focused on the free-end region are reviewed here.

Kawamura et al. (1984a) visualized the flow in the vertical symmetry plane using the smoke-wire technique for three different aspect ratios ($AR=8, 4, 1$) at $Re=1.07 \times 10^4$ (with $\delta/D=1$), with the results reproduced here in Fig. 20. Based on their interpretation of the photographs in Fig. 20, reattachment was observed for $AR=8$ (with $\delta/H=0.125$) (Fig. 20(a)) and for $AR=1$ (with $\delta/H=1$) (Fig. 20(c)), but, unusually, no clear reattachment could be observed for the intermediate case of $AR=4$ (with $\delta/H=0.25$) (Fig. 20(b)); the latter result has not been reported in any other study in the literature.

Leder (2003) used laser Doppler velocimetry (LDV) to the study the flow around a cylinder of $AR=2$ at $Re=2 \times 10^5$ (with $\delta/D=0.008$) including the flow over the free end. The mean flow field on the symmetry plane is shown in Fig. 21(a), which

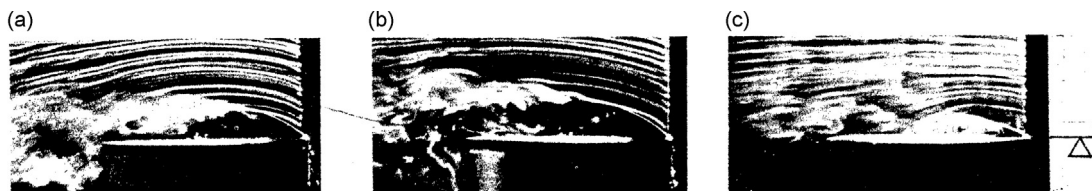


Fig. 20. Flow visualization results in the vertical symmetry plane above the free end of a surface-mounted finite-height circular cylinder, $Re=1.07 \times 10^4$, $\delta/D=1$, from Kawamura et al. (1984). Flow from right to left. (a) $AR=8$; (b) $AR=4$; (c) $AR=1$.

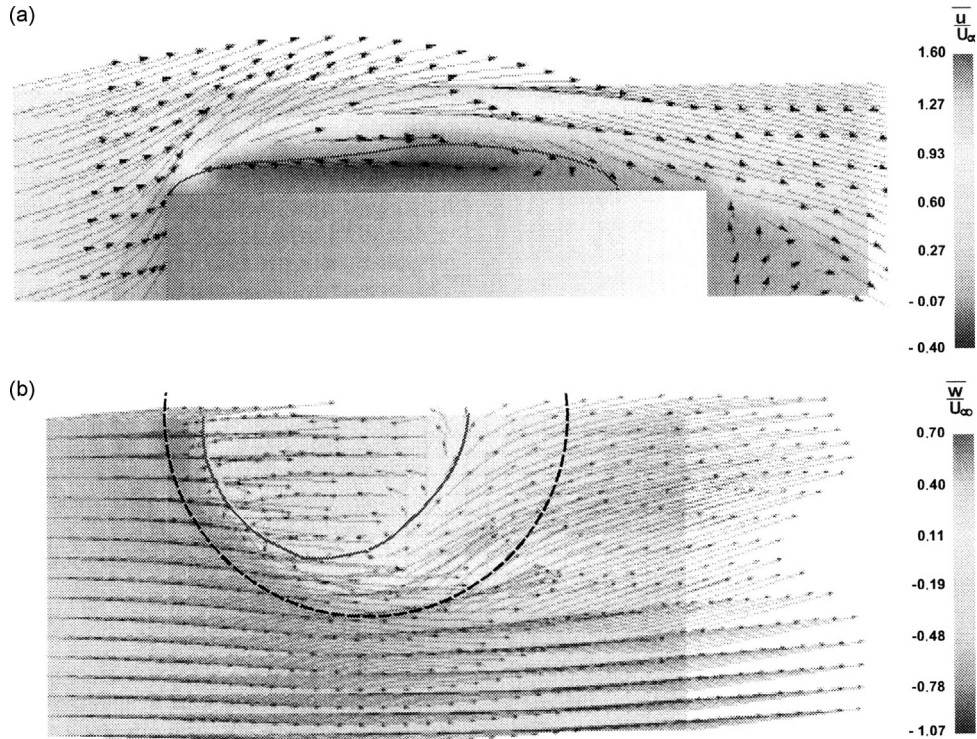


Fig. 21. LDV measurements of the mean flow above the free end of a surface-mounted finite-height circular cylinder, $AR=2$, $Re=2 \times 10^5$, $\delta/D=0.008$, from Leder (2003) (where u and w are the mean streamwise and wall-normal velocity components): (a) mean velocity field on the vertical symmetry plane ($y/D=0$); (b) mean velocity field in a horizontal plane at $z=0.05D$ above the free end.

illustrates the flow separating from the leading edge and its reattachment at $x_R/D=0.34$. There is no evidence of the leading edge separation bubble, but this feature might have been missed due to the low spatial resolution of the measurements. In Fig. 21(b), the mean flow field is shown in a horizontal plane $0.05D$ above the free end. The mean velocity vectors clearly show the recirculation zone, the reattachment line, and other flow features. Because of the low spatial resolution, however, the foci and other critical points are difficult to discern.

Pattenden et al. (2005) used PIV to study the ensemble-averaged and instantaneous behavior of the recirculation zone and the separating shear layer from the leading edge. Their mean flow results (Fig. 22(a)) show the arch (mushroom) vortex within the recirculation zone and reattachment of the shear layer onto the free-end surface. Their PIV results do not show, however, the separation bubble (and any associated small cross-stream vortex structures) just downstream of the leading edge. The instantaneous results (Fig. 22(b)) showed the dynamics of the separating shear layer and the variability in the reattachment point location.

Afgan et al. (2007) performed large eddy simulations (LES) of the flow around finite cylinders of $AR=6$ and 10 at $Re=2 \times 10^4$ (δ/D not specified in their work) and showed a single example of the flow above the free end for the case of $AR=6$, reproduced here in Fig. 23. The mean flow field from their simulations differs considerably from nearly all of the experimental results in the literature, with a reattachment point at $x_R/D \approx 0$ and no evidence of the foci or other critical points. Looking at the x_R/D data collected in Fig. 17, a reattachment point of $x_R/D \approx 0.3$ would be expected for $AR=6$. It may be that greater mesh refinement was needed near the free end to more accurately model the flow field in this region.

Tomographic and time-resolved PIV measurements by Hain et al. (2008) were made above the free end of a finite circular of $AR=2.167$ at $Re=1.1 \times 10^5$ (tomographic PIV) and $Re=1 \times 10^5$ (time-resolved PIV) with $\delta/D=0.25$. The mean flow in a horizontal plane close to the free-end surface (at $z/D=0.013$) is shown in Fig. 24(a). The high spatial resolution of the vector field shows the recirculation region, the reattachment line, and the various critical points (including the foci). Their velocity data also show the origins of streamwise tip vortices near the trailing edge of the free-end surface, which have also been reported in some of other studies (e.g., Roh and Park (2001, 2003), Palau-Salvador et al. (2010)); nodes associated with these tip vortices are not identified by Hain et al. (2008). These tip vortices trail into the near-wake region from the rear edges of the cylinder free end; a visualization of these vortices using the λ_2 -criterion is shown in Fig. 24(b). The flow in the vertical symmetry plane ($y/D=0$), in Fig. 24(c,d), shows the mean recirculation zone and the reattachment of the separated flow onto the free end from the two PIV techniques. There are some differences between the two mean flow fields near the trailing edge which can possibly be attributed to the different measurement techniques, a small difference in Reynolds numbers, and differences in the ensemble sizes; tomographic PIV showed reattachment at $x_R/D=0.29$ while the time-resolved PIV results gave $x_R/D=0.35$. Both Fig. 24(c,d) show the center of the arch (mushroom) vortex to be located quite far

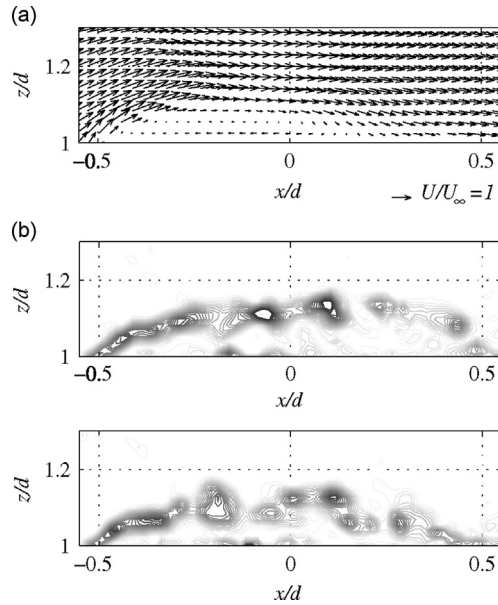


Fig. 22. PIV measurements by [Pattenden et al. \(2005\)](#) in the vertical symmetry plane above the free end of a surface-mounted finite-height circular cylinder, $AR=1$, $Re=2 \times 10^5$, $\delta/D=\delta/H=0.1$: (a) ensemble-average velocity vector field; (b) two selected instantaneous cross-stream vorticity fields. Note that in these figures the origin is at the cylinder-wall junction, d is the diameter of the cylinder, and U is the mean streamwise velocity.

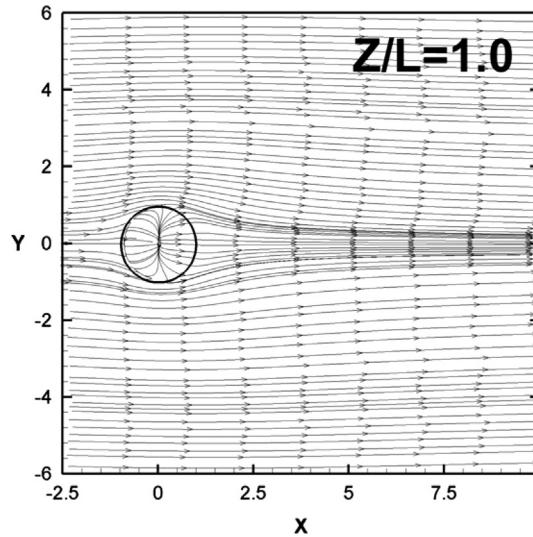


Fig. 23. Numerical solution of the flow just above the free end ($z/D \approx 0$) of a surface-mounted finite-height circular cylinder of $AR=6$, $Re=2 \times 10^4$, δ/D not specified, from [Afgan et al. \(2007\)](#). Note that in this figure the coordinate variables X and Y are given in multiples of the cylinder radius, i.e., $X=2x/D$ and $Y=2y/D$, Z is the wall-normal coordinate, and L is the height of the cylinder.

from the free-end surface. Neither figure shows any evidence of the separation bubble near the leading edge. [Hain et al. \(2008\)](#) also presented results for the in-plane Reynolds shear stress in the symmetry plane (Fig. 24(e)). An example of the instantaneous vorticity field is shown in Fig. 24(f) which is very similar to the results of [Pattenden et al. \(2005\)](#) in Fig. 22(b), with the appearance of shear-layer (Kelvin–Helmholtz) vortices. [Hain et al. \(2008\)](#) also reported periodic oscillations or “flapping” of the of the separated shear layer, with a Strouhal number of $St \approx 0.014$. This value is much lower than those reported in the earlier studies of [Kitagawa et al. \(1999, 2002\)](#) and [Park and Lee \(2000, 2002, 2004\)](#), which they attributed to the periodicity of the tip vortices.

[Palau-Salvador et al. \(2010\)](#) presented numerical simulations of the flow over finite cylinders; selected results are shown in Figs. 25 and 26 for $AR=2.5$ and $AR=5$, respectively. The mean streamlines on the vertical symmetry plane for the two aspect ratios (Figs. 25 and 26(a)) show flow separating from the leading edge, the large recirculation zone on the free-end surface, and reattachment at $x_R/D=0.38$ for $AR=2.5$ and $x_R/D=0.41$ for $AR=5$. The simulations for both aspect ratios also show the separation bubble near the leading edge, which forms as flow reversing upstream along the free-end surface

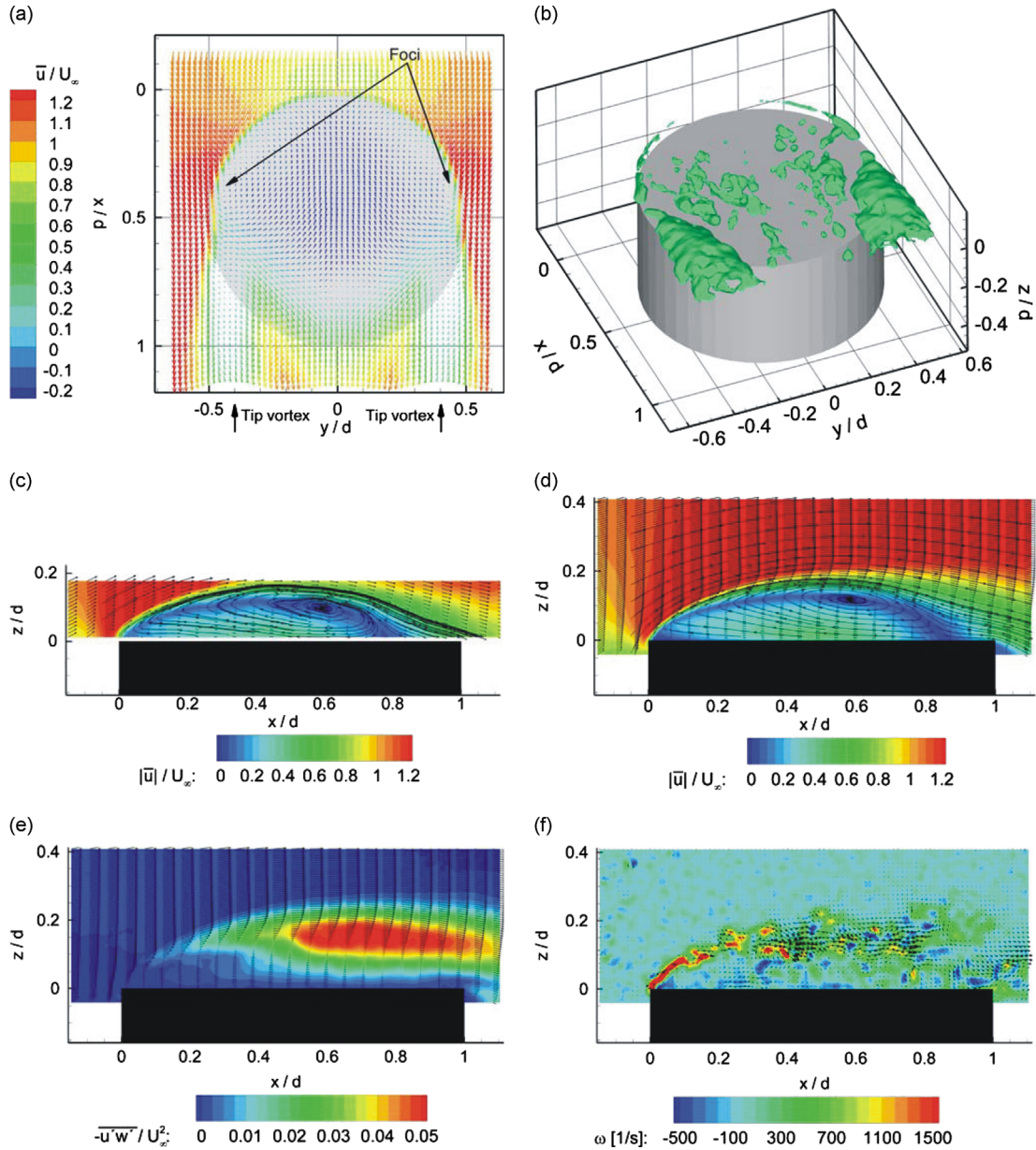


Fig. 24. Flow above a surface-mounted finite-height circular cylinder of $AR=2$, $\delta/D=0.25$, from the PIV measurements of Hain et al. (2008): (a) flow field in a horizontal plane at $z/D=0.013$ above the free-end surface (with foci located at $x/d=0.4, y/d=\pm 0.43$ using the coordinate system in the figure, where d is the cylinder diameter), tomographic PIV, $Re=1.1 \times 10^5$, where \bar{u} is the mean streamwise velocity component; (b) representation of the tip vortices using the λ_2 -criterion, showing the tip vortices originating at the side edges of the free end surface, tomographic PIV, $Re=1.1 \times 10^5$; (c) mean flow field in the vertical symmetry plane ($y/D=0$), tomographic PIV, $Re=1.1 \times 10^5$; (d) mean flow field in the vertical symmetry plane ($y/D=0$), time-resolved PIV, $Re=1 \times 10^5$; (e) Reynolds shear stress in the vertical symmetry plane ($y/D=0$), time-resolved PIV, $Re=1 \times 10^5$; (f) instantaneous in-plane vorticity field in the vertical symmetry plane ($y/D=0$), time-resolved PIV, $Re=1 \times 10^5$. Note that in these figures, the x -coordinate begins at the leading edge of the cylinder.

separates from the surface before reaching the leading edge. The mean streamline patterns in horizontal planes above the free end surface (Fig. 25(b,c)) are similar to the oil flow visualization patterns presented earlier: the results for $z=0.046D$ above the surface (Fig. 25(c)) show the pair of foci, the reattachment line, the recirculation zone, and the reattachment and separation saddle points on the centerline. For the flow pattern closer to the surface, at $z=0.0015D$, additional flow features become visible, including a nodal point on the centerline just downstream of the leading edge, and two other nodal points near the trailing edge on either side of the cylinder. The nodal point downstream of the leading edge is identified as point “A1” in the enlargement (Fig. 25(d)). The other two nodal points are similar to what was seen by Roh and Park (2001, 2003) (Fig. 10) and suggested by Rödiger et al. (2007). The enlargement in Fig. 25(d) also shows the small vortex structures in the symmetry plane near the leading edge. A prominent clockwise vortex is seen above the free-end surface, whereas

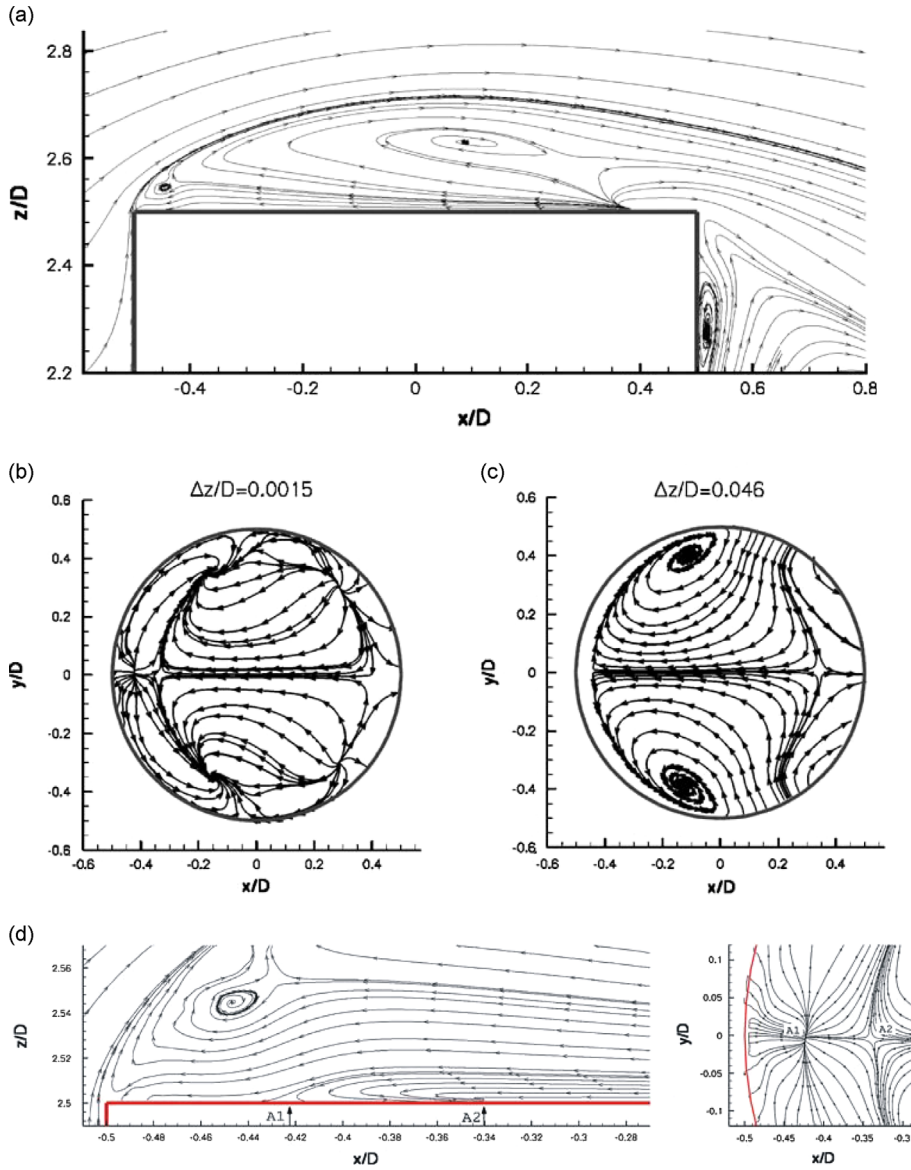


Fig. 25. Numerical (LES) simulation results for the flow over a surface-mounted finite-height circular cylinder of $AR=2.5$, $Re=4.3 \times 10^4$, $\delta/D=0.313$, from Palau-Salvador et al. (2010): (a) mean flow in the vertical symmetry plane ($y/D=0$) (note the z -coordinate begins at the ground plane); (b,c) mean streamline patterns in horizontal planes above the free-end surface; (d) close-up of the flow near the leading edge.

the counter-clockwise vortex co-located with critical point “A2” (the separation saddle point), and associated with the separation bubble, is rather small and compressed close to the free-end surface. This two-vortex pattern near the leading edge was a feature of the flow models of Hölscher and Niemann (1996) (Fig. 6) and Donnert et al. (2007) (Fig. 13).

Further insight into the flow above the free end was given in the recent numerical simulations by Krajnović (2011) for a finite circular cylinder of $AR=6$ at $Re=2 \times 10^4$. Examples of the flow from his simulations are shown in Figs. 27 and 28. Key time-averaged flow features identified on the free end include the mean recirculation zone and the main cross-stream arch (mushroom) vortex (labeled “V_{f1}” in Figs. 27 and 28). As shown in Fig. 27, the axis of this vortex bends near the ends to terminate on the free end surface near the sides of the cylinder, as also conjectured in the earlier studies of Kawamura et al. (1984a,b) and Pattenden et al. (2005, 2006). The ends of this vortex are denoted by two focal points (labeled “F1” and “F2” in Fig. 27(b)) in the mean streamlines near the surface. The vortex line is sketched in Figs. 27 and 28. A second, smaller cross-stream vortex is also shown (labeled “V_{f2}” in Figs. 27 and 28) within a secondary recirculation region that forms downstream of the leading edge, referred to in other studies as the separation bubble (Tsutsui, 2012; Fig. 15). The evidence for this vortex has been suggested in some studies, such as the models of Hölscher and Niemann (1996) (Fig. 7) and Donnert et al. (2007) (Fig. 13), which show a pair of vortices, and the simulations by Palau-Salvador et al. (2010) (Figs. 25 and 26). Also seen in Krajnović’s (2011) simulations are the free-end surface topology (Figs. 27 and 28), with a reattachment saddle

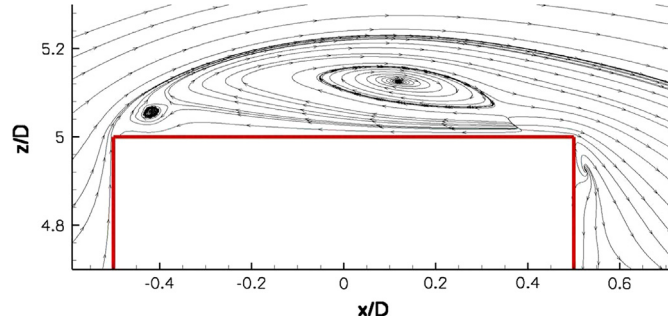


Fig. 26. Numerical (LES) simulation results for the flow over a surface-mounted finite-height circular cylinder of $AR=5$, $Re=2.2 \times 10^4$, $\delta/D=0.625$, from Palau-Salvador et al. (2010), showing the mean flow in the vertical symmetry plane ($y/D=0$) (note the z -coordinate begins at the ground plane). A single cross-stream vortex with clockwise sense of rotation is seen in the separation bubble downstream of the leading edge.

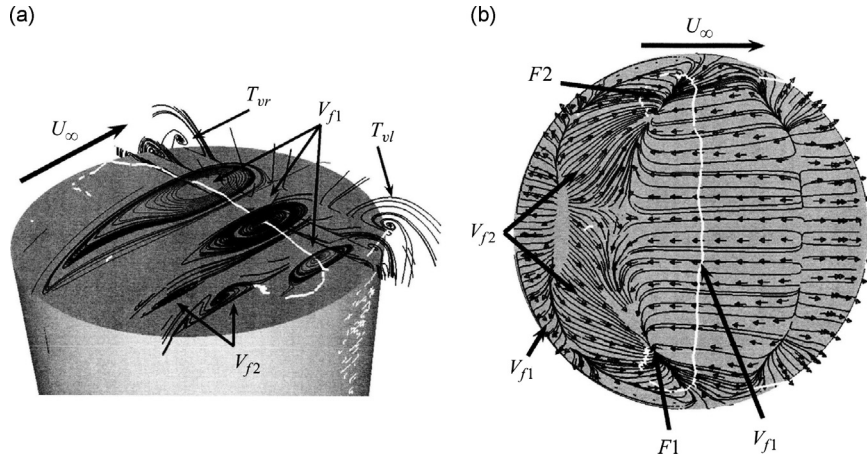


Fig. 27. Free-end flow topology and vortex patterns for a surface-mounted finite-height circular cylinder of $AR=6$, $Re=2 \times 10^4$, $\delta/D=0.07$, from the numerical (LES) simulations of Krajnović (2011): (a) mean streamlines above the free end, showing the main arch vortex (V_{f1}), the leading edge separation bubble characterized by a single cross-stream vortex V_{f2} , and trailing vortices T_{vl} and T_{vr} ; (b) surface streamlines showing focal points $F1$ and $F2$ at the termination points of the arch vortex.

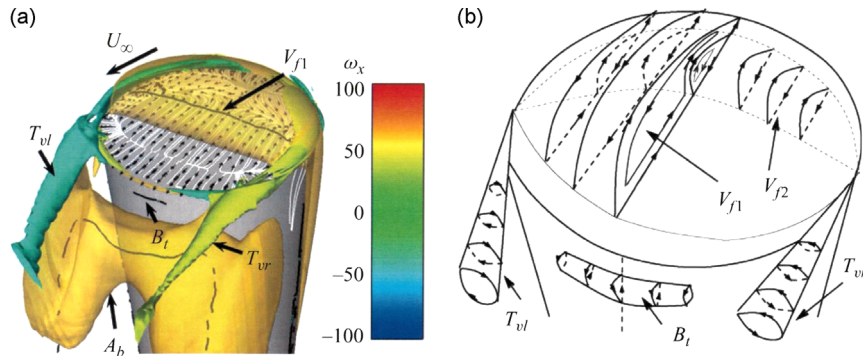


Fig. 28. Free-end flow topology and vortex patterns for a surface-mounted finite-height circular cylinder of $AR=6$, $Re=2 \times 10^4$, $\delta/D=0.07$, from the numerical (LES) simulations of Krajnović (2011): (a) isosurfaces of mean streamwise vorticity (ω_x) showing the left and right tip vortices (labeled T_{vl} and T_{vr}) which may be originating from nodes on the free-end surface near the trailing edge; (b) schematic of the mean vortex structures on the free-end surface, including the cross-stream arch vortex (V_{f1}), leading edge separation bubble vortex (V_{f2}), and the tip vortices (T_{vl} and T_{vr}).

point on the centerline, a dividing (reattachment) streamline closer to the rear of the free-end surface, and a separation saddle point just downstream of the leading edge close to where “ V_{f2} ” is observed. Two nodes may also be discerned closer to the trailing edge of the free-end surface (Fig. 27(b)) from which the trailing vortices (labeled “ T_{vl} ” and “ T_{vr} ” in Figs. 27 and 28) originate and subsequently enter the wake (Fig. 28(a)); this would be consistent with some aspects of the model of Roh and Park (2001, 2003) and the suggestions of Rödiger et al. (2007). Fig. 28(b) shows an overall schematic of the time-averaged vortex structures associated with the free end.

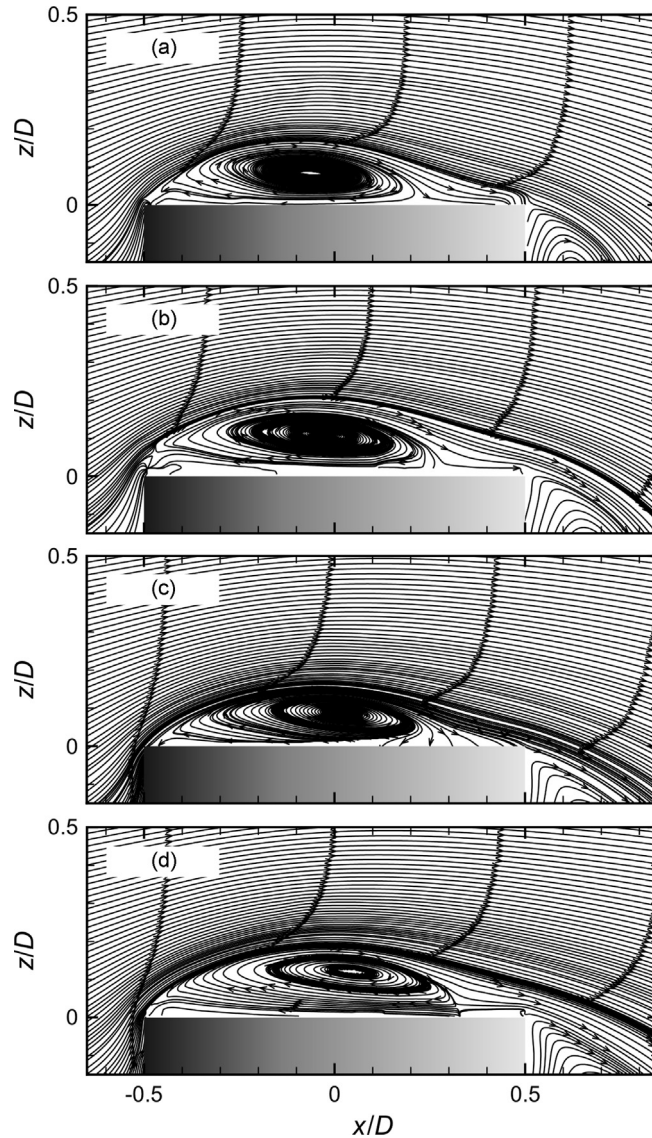


Fig. 29. Mean streamlines in the vertical symmetry plane about the free end of a surface-mounted finite-height circular cylinder (from [Rostamy et al., 2012](#)), $Re = 4.2 \times 10^4$, $\delta/D = 1.6$: (a) $AR = 9$; (b) $AR = 7$; (c) $AR = 5$; (d) $AR = 3$. Note that in this figure, the vertical coordinate z begins at the ground plane.

Recent PIV experiments by [Rostamy et al. \(2012\)](#) provided results for the mean recirculation zone in the vertical symmetry plane for finite circular cylinders of $AR = 9, 7, 5$, and 3 at $Re = 4.2 \times 10^4$ with $\delta/D = 1.7$ ([Fig. 29](#)). For this range of aspect ratios, as AR decreased, the location of the reattachment saddle point moved gradually towards the trailing edge. This result contrasted with the behavior at lower aspect ratio, as shown in [Fig. 17](#); however, there is a general absence of data in the literature at higher AR . [Rostamy et al. \(2012\)](#) did not observe significant differences to the mean recirculation zone with AR , even for the case of $AR = 3$ which was below the critical aspect ratio.

The results shown in [Figs. 25\(a\), 26, 28\(b\)](#) and [29](#) illustrate some of the interconnection between the flow above the free-end surface and the flow in the near-wake region. For example, mean flow leaving the trailing edge of the free-end surface becomes entrained into the mean cross-stream vortex structure (vortex “B_t” in [Fig. 28](#)) that forms in the upper part of the near wake just downstream of the leading edge. However, a complete picture showing the link between the free-end flow field and the near wake is generally lacking in the literature.

7. Conclusions

This review article is an attempt to summarize the literature pertaining to the flow above the free end of a surface-mounted finite-height circular cylinder, looking at the effects of aspect ratio and relative boundary layer thickness. Several schematics or models have been presented in the literature, most of which agree on the basic elements of the mean flow

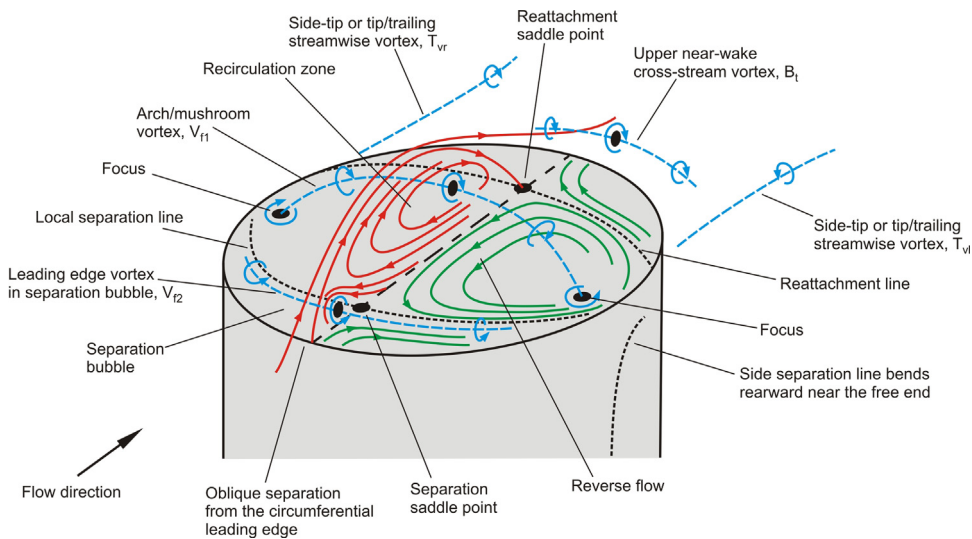


Fig. 30. Schematic of the free-end flow field for higher-aspect-ratio surface-mounted finite-height circular cylinders showing the main flow features.

field on the free-end surface: separation of the approach flow from the circumferential leading edge of the free-end surface; formation of mean recirculation zone on the free-end surface, which contains a mean cross-stream “arch” or “mushroom” vortex; reattachment of the separated flow onto the free-end surface along a prominent reattachment line, which lies closer to the leading edge as the aspect ratio becomes smaller; a reattachment saddle point on the centerline; and a bending of the arch vortex axis on either side of the centerline such that vortex terminates at two foci on the free-end surface.

Apart from the location of the reattachment point, the influences of Reynolds number, aspect ratio and relative boundary layer thickness are not well understood, particularly for high-aspect-ratio cylinders above the critical aspect ratio; most of the experiments in the literature have been concentrated on cylinders of relatively low aspect ratio, $AR \leq 2$, and there is a need for additional studies at higher AR. Additional studies would help clarify the influence of the critical aspect ratio and how it influences (or not) the free-end flow field. Further explanation is also needed on how free-end flow field interacts with the near wake and its vortex patterns.

Several other free-end flow features are not universally seen in all experiments and simulations: a small mean separation bubble near the leading edge, formed as the reversing flow in the main recirculation zone locally separates from the surface; one or two small cross-stream vortices within this separation bubble; formation of “side-tip” vortices from the free-end surface, either from the side edges of the free end or from nodes on the free-end surface; formation of the streamwise tip or trailing vortices from various locations on the body or in the near-wake. The reasons for not observing these features may include a general lack of understanding of Reynolds number, aspect ratio and boundary layer effects; misinterpretation of surface oil flow visualization experiments and flow topology; reliance on time-averaged representations of the flow field rather than phase-averaged or instantaneous data; low spatial resolution of pressure, heat transfer, and near-surface velocity measurements; and/or lack of grid refinement for numerical simulations. More time-resolved measurements would allow the origins of the periodicities associated with the free-end flow field to be better explained.

Based on the literature review, an overall schematic of the free-end flow field for higher-aspect-ratio cylinders is offered in Fig. 30, where many of the main flow features are identified. Some of the flow features illustrated in Fig. 30 remain speculative and need additional experiments or simulations to verify their existence or structure, in particular the separation bubble, the number of cross-stream vortices contained within this bubble and their termination points, and the origin of the side-tip or trailing vortices.

Acknowledgments

Support from the Natural Sciences and Engineering Research Council of Canada (NSERC) is gratefully acknowledged.

References

- Adaramola, M.S., Akinlade, O.J., Sumner, D., Bergstrom, D.J., Schenstead, A.J., 2006. Turbulent wake of a finite circular cylinder of small aspect ratio. *Journal of Fluids and Structures* 22, 919–928.
- Afgan, I., Moulinec, C., Prosser, R., Laurence, D., 2007. Large eddy simulation of turbulent flow for wall mounted cantilever cylinders of aspect ratio 6 and 10. *International Journal of Heat and Fluid Flow* 28, 561–574.
- Agui, J.H., Andreopoulos, J., 1992. Experimental investigation of a three-dimensional boundary layer flow in the vicinity of an upright wall mounted cylinder. *ASME Journal of Fluids Engineering* 114, 566–576.

- Bourgeois, J.A., Sattari, P., Martinuzzi, R.J., 2011. Alternating half-loop shedding in the turbulent wake of a finite surface-mounted square cylinder with a thin boundary layer. *Physics of Fluids* 23 (095101), 15.
- Chen, Z., Hosseini, Z., Martinuzzi, R., 2012. The influence of boundary layer state on the wake topology of a surface mounted bluff body. In: *Proceedings of 20th Annual Conference of the CFD Society of Canada, CFD2012*, Canmore, AB, Canada, May 9–11, 2012, 6 pp.
- Dobriloff, C., Nitsche, W., 2009. Surface pressure and wall shear stress measurements on a wall mounted cylinder. In: Nitsche, W., Dobriloff, C. (Eds.), *Imaging Measurement Methods, NNFM 106*, Springer-Verlag, Berlin, pp. 197–206.
- Donnert, G.D., Kappler, M., Rodi, W., 2007. Measurement of tracer concentration in the flow around finite-height cylinders. *Journal of Turbulence* 8 (No. 33), 18.
- Einian, M., Bergstrom, D.J., Sumner, D., 2010. Numerical simulation of the flow around a surface-mounted square cylinder. In: *Proceedings of the ASME 2010 3rd Joint US-European Fluids Engineering Summer Meeting and 8th International Conference on Nanochannels, Microchannels, and Minichannels (FEDSM2010-ICNMM2010)*, August 1–5, 2010, Montreal, QC, Canada, Paper No. FEDSM-ICNMM2010-30394, 8 pp.
- Etzold, F., Fiedler, H., 1976. The near-wake structure of a cantilevered circular cylinder in a cross-flow. *Zeitschrift fuer Flugwissenschaften* 24, 77–82.
- Fox, T.A., Apelt, C.J., West, G.S., 1993. The aerodynamic disturbance caused by the free-ends of a circular cylinder immersed in a uniform flow. *Journal of Wind Engineering and Industrial Aerodynamics* 49, 389–400.
- Frederich, O., Wassen, E., Thiele, F., Jensch, M., Brede, M., Huttman, F., Leder, A., 2007. Numerical simulation of the flow around a finite cylinder with ground plate in comparison to experimental measurements. In: Tropea, V. (C., et al. (Eds.), *New Research in Numerical and Experimental Fluid Mechanics, NNFM 96*, Springer-Verlag, Berlin, pp. 348–355.
- Gould, R.W.E., Raymer, W.G., Ponsford, P.J., 1968. Wind tunnel tests on chimneys of circular section at high Reynolds numbers. In: Johns, D.J., Scruton, C., Ballantyne, A.M. (Eds.), *Proceedings of a Symposium on Wind Effects on Buildings and Structures*, April 2–4, 1968, Loughborough University of Technology, UK, pp. 10.1–10.17.
- Hain, R., Kähler, C.J., Michaelis, D., 2008. Tomographic and time resolved PIV measurements on a finite cylinder mounted on a flat plate. *Experiments in Fluids* 45, 715–724.
- Hiwada, M., Kawamura, T., Hibino, T., Mabuchi, I., Kumada, M., 1984. Heat transfer from a finite circular cylinder on a flat plate: in the case of cylinder length larger than the turbulent boundary layer thickness. *Transactions of the JSME* 50, 733–742. (in Japanese).
- Hölscher, N., Niemann, H.J., 1996. Turbulence and separation induced pressure fluctuations on a finite circular cylinder – application of a linear unsteady strip theory. *Journal of Wind Engineering and Industrial Aerodynamics* 65, 335–346.
- Iungo, G.V., Pii, L.M., Buresti, G., 2012. Experimental investigation on the aerodynamic loads and wake flow features of a low aspect-ratio circular cylinder. *Journal of Fluids and Structures* 28, 279–291.
- Johnston, C.R., Wilson, D.J., 1996. A vortex pair model for plume downwash into stack wakes. *Atmospheric Environment* 31, 13–20.
- Kappler, M., 2002. Experimentelle Untersuchung der Umströmung von Kreiszyllindern mit ausgeprägten dreidimensionalen Effekten (Ph.D. thesis). Institut für Hydromechanik, Universität Karlsruhe, Germany (in German).
- Kawamura, T., Hiwada, M., Hibino, T., Mabuchi, T., Kumada, M., 1984a. Flow around a finite circular cylinder on a flat plate. *Bulletin of the JSME* 27, 2142–2150.
- Kawamura, T., Hiwada, M., Hibino, T., Mabuchi, T., Kumada, M., 1984b. Flow around a finite circular on flat plate: in the case of cylinder length larger than turbulent boundary layer thickness. *Transactions of the JSME* 50, 332–341. (in Japanese).
- Kawamura, T., Hiwada, M., Hibino, T., Mabuchi, T., Kumada, M., 1984c. Heat transfer from a finite circular cylinder on the flat plate. *Bulletin of the JSME* 27, 2430–2439.
- Kitagawa, T., Fujino, Y., Kimura, K., 1999. Effects of free end condition on end-cell-induced vibration. *Journal of Fluids and Structures* 13, 499–518.
- Kitagawa, T., Fujino, Y., Kimura, K., Mizuno, Y., 2002. Wind pressures measurement on end-cell-induced vibration of a cantilevered circular cylinder. *Journal of Wind Engineering and Industrial Aerodynamics* 90, 395–405.
- Krajnović, S., 2011. Flow around a tall finite cylinder explored by large eddy simulation. *Journal of Fluid Mechanics* 676, 294–317.
- Leder, A., 2003. 3D-flow structures behind truncated circular cylinders. In: *Proceedings of ASME FEDSM'03, 4th ASME-JSME Joint Fluids Engineering Conference*, July 6–10, 2003, Honolulu, Hawaii, USA, Paper No. FEDSM2003-45083, 7 pp.
- Lee, L.W., 1997. Wake structure behind a circular cylinder with a free end. In: *Proceedings of the Heat Transfer and Fluid Mechanics Institute*, pp. 241–251.
- Majumdar, S., Rodi, W., 1989. Three-dimensional computation of flow past cylindrical structures and model cooling towers. *Building and Environment* 24, 3–22.
- Okamoto, S., Sunabashiri, Y., 1992. Vortex shedding from a circular cylinder of finite length placed on a ground plane. *ASME Journal of Fluids Engineering* 114, 512–521.
- Okamoto, T., Yagita, M., 1973. The experimental investigation on the flow past a circular cylinder of finite length placed normal to the plane surface in a uniform stream. *Bulletin of the JSME* 16, 805–814.
- Palau-Salvador, G., Stoesser, T., Fröhlich, J., Kappler, M., Rodi, W., 2010. Large eddy simulations of flow around finite-height cylinders. *Flow, Turbulence and Combustion* 84, 239–275.
- Park, C.W., Lee, S.J., 2000. Free end effects on the near wake flow structure behind a finite circular cylinder. *Journal of Wind Engineering and Industrial Aerodynamics* 88, 231–246.
- Park, C.W., Lee, S.J., 2002. Flow structure around a finite circular cylinder embedded in various atmospheric boundary layers. *Fluid Dynamics Research* 30, 197–215.
- Park, C.W., Lee, S.J., 2004. Effects of free-end corner shape on flow structure around a finite cylinder. *Journal of Fluids and Structures* 19, 141–158.
- Pattenden, R.J., Turnock, S.R., Zhang, X., 2005. Measurements of the flow over a low-aspect-ratio cylinder mounted on a ground plane. *Experiments in Fluids* 39, 10–21.
- Pattenden, R.J., Turnock, S.R., Zhang, X., 2006. Unsteady simulations of the flow around a short surface-mounted cylinder. *International Journal for Numerical Methods in Fluids* 53, 895–914.
- Rödiger, T., Knauss, H., Gaisbauer, U., Krämer, E., 2007. In: Tropea, C., et al. (Eds.), *New Research in Numerical and Experimental Fluid Mechanics VI, NNFM 96*, Springer-Verlag, Berlin, pp. 121–128.
- Roh, S.C., Park, S.O., 2001. Surface flow pattern and local mass transfer on the free-end surface of a finite circular cylinder. *Heat and Mass Transfer* 38, 1–5.
- Roh, S.C., Park, S.O., 2003. Vortical flow over the free end surface of a finite circular cylinder mounted on a flat plate. *Experiments in Fluids* 34, 63–67.
- Rostamy, N., Sumner, D., Bergstrom, D.J., Bugg, J.D., 2012. Local flow field of a surface-mounted finite circular cylinder. *Journal of Fluids and Structures* 34, 105–122.
- Sakamoto, H., Arie, M., 1983. Vortex shedding from a rectangular prism and a circular cylinder placed vertically in a turbulent boundary layer. *Journal of Fluid Mechanics* 126, 147–165.
- Sattari, P., Bourgeois, J.A., Martinuzzi, R.J., 2012. On the vortex dynamics in the wake of a finite surface-mounted square cylinder. *Experiments in Fluids* 52, 1149–1167.
- Sparrow, E.M., Samie, F., 1981. Measured heat transfer coefficients at an adjacent to the tip of a wall-attached cylinder in crossflow—application to fins. *ASME Journal of Heat Transfer* 103, 778–784.
- Sumner, D., Heseltine, J.L., Dansereau, O.J.P., 2004. Wake structure of a finite circular cylinder of small aspect ratio. *Experiments in Fluids* 37, 720–730.
- Tanaka, S., Murata, S., 1999. An investigation of the wake structure and aerodynamic characteristics of a finite circular cylinder. *JSME International Journal, Series B: Fluids Thermal Engineering* 42, 178–187.
- Taneda, S., 1952. An experimental study on the structure of the vortex street behind a circular cylinder of finite length. *Reports of the Research Institute for Applied Mechanics* 1, 131–144.
- Taniguchi, S., Sakamoto, H., Arie, M., 1981. Flow around circular cylinders of finite height placed vertically in turbulent boundary layers. *Bulletin of the JSME* 24, 37–44.

- Tsutsui, T., 2012. Flow around a cylindrical structure mounted in a plane turbulent boundary layer. *Journal of Wind Engineering and Industrial Aerodynamics* 104–106, 239–247.
- Tsutsui, T., Igarashi, T., Nakamura, H., 2000. Fluid flow and heat transfer around a cylindrical protuberance mounted on a flat plate boundary layer. *JSME International Journal Series B* 43, 279–287.
- Tsutsui, T., Kawahara, M., 2006. Heat transfer around a cylindrical protuberance mounted in a plane turbulent boundary layer. *ASME Journal of Heat Transfer* 128, 153–161.
- Wang, H.F., Zhou, Y., 2009. The finite-length square cylinder near wake. *Journal of Fluid Mechanics* 638, 453–490.
- Wang, H.F., Zhou, Y., Chan, C., Lam, K.S., 2006. Effect of initial conditions on interaction between a boundary layer and a wall-mounted finite-length-cylinder wake. *Physics of Fluids* 18 (065106), 12.
- Wang, H.F., Zhou, Y., Mi, J., 2012. Effects of aspect ratio on the drag of a wall-mounted finite-length cylinder in subcritical and critical regimes. *Experiments in Fluids* 53, 423–436.